

Cite this: *J. Mater. Chem. A*, 2024, 12, 23202

## Recent progress on electrocatalysts in ammonia electrooxidation reaction for clean hydrogen production

N. S. Hassan,<sup>ab</sup> A. A. Jalil,<sup>id</sup> \*<sup>ab</sup> R. Saravanan,<sup>id</sup> <sup>c</sup> N. M. Izzuddin,<sup>id</sup> <sup>b</sup> M. B. Bahari,<sup>d</sup> D. Prasetyoko<sup>id</sup> <sup>e</sup> and R. E. Nugraha<sup>f</sup>

Hydrogen (H<sub>2</sub>) is considered one of the most promising alternative energy resources, serving as a clean energy carrier, replacing fossil fuels. Ammonia (NH<sub>3</sub>) is recognized as a high-potential H<sub>2</sub> carrier and is utilized as a primary material for H<sub>2</sub> production. The NH<sub>3</sub> electro-oxidation reaction (AOR) is crucial for both direct NH<sub>3</sub> fuel cells and NH<sub>3</sub> electrolysis. Nevertheless, AOR frequently encounters difficulties including a high overpotential, sluggish reaction rates, and catalyst deactivation as a result of its slow kinetics, even though it is thermodynamically advantageous. In order to overcome these obstacles, numerous approaches have been suggested for the creation of electrocatalysts that can sustain a strong reaction rate even when exposed to low overpotential. The kinetics, mechanisms, and experimental methods of AOR are the primary focus of this overview. It also examines recent advancements in electrocatalyst modifications, with a particular emphasis on single-atom electrocatalysts and transition metal-based catalysts. Additionally, the paper discusses the techno-economic assessment of the AOR reaction for H<sub>2</sub> production. Furthermore, future perspectives and recommendations for electrocatalyst development in AOR are provided. Proposing and designing new, resilient electrocatalysts will be significantly aided by the fundamentals and efforts detailed in this review; this, in turn, will propel advancements in AOR for practical applications.

Received 26th April 2024  
Accepted 29th July 2024

DOI: 10.1039/d4ta02897j

rsc.li/materials-a

## Introduction

Fossil fuels, notably coal, oil, and natural gas, have historically served as primary energy sources across various sectors, such as electricity generation, transportation, and industrial processes. However, their finite nature, coupled with significant environmental and social externalities, underscores the imperative for transitioning towards renewable and alternative energy sources. Amidst this transition, hydrogen (H<sub>2</sub>) has emerged as a versatile energy carrier with the potential to decarbonize multiple sectors of the economy, including industry, transportation, and power generation.<sup>1,2</sup> While H<sub>2</sub> can be produced through diverse pathways, including electrolysis of water using renewable electricity,<sup>3</sup> biomass gasification,<sup>4</sup> and steam reforming of natural

gas coupled with carbon capture and storage,<sup>5</sup> conventional methods often entail carbon-intensive processes or rely on non-renewable resources thus undermining the environmental benefits of H<sub>2</sub> as a clean energy vector.

In this context, the electrooxidation of ammonia (NH<sub>3</sub>) presents a promising pathway toward sustainable H<sub>2</sub> production, addressing both environmental and technical challenges associated with conventional methods.<sup>6,7</sup> By harnessing the electrochemical reactivity of NH<sub>3</sub>, researchers endeavour to develop efficient and scalable technologies for on-demand H<sub>2</sub> generation, thereby contributing to the transition towards a low-carbon, H<sub>2</sub>-based economy. Notably, NH<sub>3</sub> electrooxidation can be conducted under mild conditions, obviating the need for high temperatures and pressures inherent in conventional steam reforming processes.<sup>8</sup> This condition reduces energy consumption and enhances process safety and operational flexibility.

The progression of publications focusing on the electro-oxidation of NH<sub>3</sub> from 2008 to 2024, depicted in Fig. 1, underscores the increasing research interest in this area. Notably, 449 documents, including articles, review articles, proceeding papers, and book chapters, have comprehensively explored various aspects of NH<sub>3</sub> electrooxidation over the past 16 years. The surge in publications since 2010 is indicative of significant advancements in research techniques and the perceived

<sup>a</sup>Centre of Hydrogen Energy, Institute of Future Energy, 81310 UTM Johor Bahru, Johor, Malaysia. E-mail: aishahaj@utm.my

<sup>b</sup>Faculty of Chemical and Energy Engineering, Universiti Teknologi Malaysia, 81310 UTM Johor Bahru, Johor, Malaysia

<sup>c</sup>Instituto de Alta Investigación, Universidad de Tarapacá, Arica-1000000, Chile

<sup>d</sup>Faculty of Science, Universiti Teknologi Malaysia, 81310 UTM Johor Bahru, Johor, Malaysia

<sup>e</sup>Department of Chemistry, Faculty of Science and Data Analytics, Institut Teknologi Sepuluh Nopember, Keputih, Sukolilo, Surabaya 60111, Indonesia

<sup>f</sup>Department of Chemical Engineering, Faculty of Engineering, Universitas Pembangunan Nasional "Veteran" Jawa Timur, Surabaya, East Java 60294, Indonesia



Fig. 1 Publication trends in the area of electrooxidation of NH<sub>3</sub> within 2008–2024.

potential applications of NH<sub>3</sub> electrooxidation in energy conversion, environmental remediation, and chemical synthesis. This surge is also reflected in the increase in citations by 2023. Furthermore, the overlay visualization in Fig. 2 highlights key terms such as “electrooxidation” and “electrochemical oxidation,” which stand out with the most significant node sizes, indicating their high frequency of occurrence. Additionally, terms represented by yellow nodes, such as catalysts, electrocatalysts, oxidation, mechanism, and fuel cell, underscore the primary focus of current research.

Indeed, designing electrocatalysts is pivotal in enhancing the efficiency and selectivity of NH<sub>3</sub> electrooxidation. Various materials and strategies have been developed to produce efficient catalysts to replace platinum (Pt),<sup>9</sup> which is costly and scarce. Researchers have explored transition metal-based catalysts, such as nickel (Ni),<sup>10,11</sup> cobalt (Co),<sup>12</sup> and iron (Fe),<sup>13</sup> as promising alternatives due to their abundance and lower cost compared to Pt. Additionally, alloying different metals or incorporating dopants into these materials has been investigated to enhance their catalytic activity and stability. Furthermore, non-metallic materials, such as carbon-based<sup>14</sup> and metal nitrides<sup>15</sup> catalysts have also shown potential for AOR. These

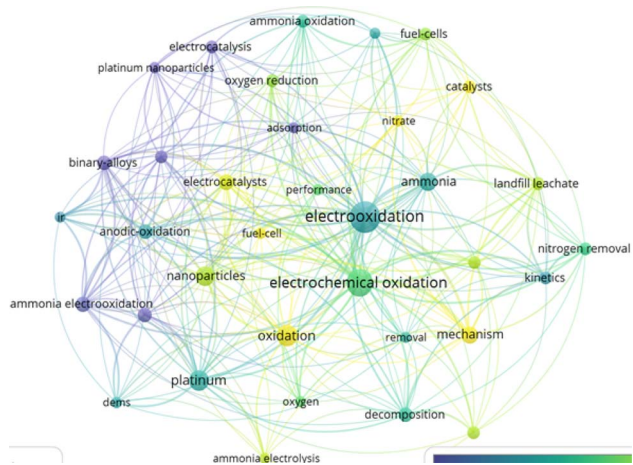


Fig. 2 Overlay visualization of most frequent terms attained via VOSViewer v.1.6.19.

materials offer advantages such as high surface area, tunable electronic properties, and chemical stability, making them attractive candidates for electrocatalysis.<sup>16,17</sup> Moreover, nanostructuring and surface engineering techniques have been employed to optimize the morphology and active sites of catalyst materials, further improving their performance in catalysing NH<sub>3</sub> electrooxidation.

Although many reviews cover catalyst development, this review will focus specifically on recent progress in electrocatalyst development to enhance AOR performance. The review will explore the various materials and strategies explored for electrocatalyst design, including single-atom electrocatalysts and transition metal-based catalysts. Additionally, the review will include a techno-economic analysis, assessing the feasibility and cost-effectiveness of different production methods of H<sub>2</sub> for large-scale implementation. Furthermore, the review will discuss the future perspectives and recommendations in electrocatalyst development for AOR. Overall, this review aims to provide insights into the state-of-the-art electrocatalyst design for improving the efficiency and selectivity of NH<sub>3</sub> electrooxidation, contributing to the advancement of sustainable H<sub>2</sub> production technologies.

## Ammonia (NH<sub>3</sub>) electrolysis for green hydrogen (H<sub>2</sub>) production

The utilization of NH<sub>3</sub> as a H<sub>2</sub> carrier undoubtedly is one of the exceptional approaches for the *in situ* production of H<sub>2</sub> fuel. This approach is also noted to exhibit minimal greenhouse gaseous (GHGs) or any hazardous compounds. Besides, NH<sub>3</sub> also displays a promising candidate material for large-scale H<sub>2</sub> production attributed to its high stability and significant capacity for H<sub>2</sub> storage.<sup>18</sup> Concerning these intrinsic features, the production of H<sub>2</sub> from NH<sub>3</sub> has attracted considerable attention and has been deeply studied for its practicability, especially in the industrial process. Interestingly, the transformation of NH<sub>3</sub> to H<sub>2</sub> can be realized using two distinct pathways which are thermal decomposition and electrolysis approaches. Even though the thermal decomposition method is well-known for being more economical compared to electrolysis, the efficiency of this method yet is still inferior to that of the electrolysis method.<sup>19</sup> Moreover, using the high temperature for the decomposition of NH<sub>3</sub> to H<sub>2</sub> and nitrogen constituents will be vulnerable to the formation of GHGs such as nitrous compounds. On the other hand, the electrolysis of NH<sub>3</sub> provides a promising interest in the field of H<sub>2</sub> production. This method utilizes a green technology with no GHGs emissions and it also can achieve high efficiency when powered by renewable energy. The efficiency of this approach also can be further enhanced depending on the advancement of the technology used. Furthermore, thermodynamic calculations demonstrated that the conversion of NH<sub>3</sub> to nitrogen and H<sub>2</sub> requires a negligible quantity of external energy (0.06 V), which is significantly less than the energy demanded by water electrolysis (1.23 V).<sup>20</sup> Theoretically, this indicates that the NH<sub>3</sub> to H<sub>2</sub> conversion is more energy-efficient than water-splitting.<sup>21</sup>

Generally, the electrolysis of water using renewable electricity and the electrooxidation of ammonia are two distinct processes with different objectives, methodologies, and challenges. The primary purpose of water electrolysis is to produce H<sub>2</sub> and O<sub>2</sub> gases.<sup>22</sup> This process involves splitting water into its constituent elements using an electrical current, with the reaction: 2H<sub>2</sub>O → 2H<sub>2</sub> + O<sub>2</sub>. The H<sub>2</sub> produced can be used as a clean fuel for various applications, including fuel cells, chemical synthesis, and energy storage. Typically, noble metal catalysts such as platinum (Pt), iridium (Ir), and ruthenium (Ru) are used in this process due to their high activity and stability. The process can utilize either acidic or alkaline electrolytes, and it usually operates at elevated temperatures and pressures to enhance efficiency and gas production rates.<sup>23</sup> The efficiency of water electrolysis systems ranges from 60% to 80%, depending on the specific technology and operating conditions. However, the process requires a high energy input, and challenges include catalyst degradation and overpotential losses. Despite these challenges, water electrolysis is highly suitable for integration with renewable energy sources like solar and wind power, allowing for the storage of intermittent renewable energy in the form of H<sub>2</sub> gas. The environmental impact is minimal, as water is the only by-product, making it a sustainable and environmentally friendly process.

In contrast, the primary purpose of NH<sub>3</sub> electrooxidation is to convert NH<sub>3</sub> to N<sub>2</sub> gas and water helping to treat ammonia-containing waste and reduce environmental pollution. This process typically uses transition metal catalysts such as Pt, Ni, and Cu, which facilitate the oxidation of NH<sub>3</sub>. It generally operates at ambient temperature and pressure, making it less energy-intensive than water electrolysis. The efficiency of NH<sub>3</sub> electrooxidation depends on the catalyst used and the reaction conditions. Significant challenges include NH<sub>3</sub> slip (unreacted ammonia), the formation of unwanted by-products, and electrode poisoning. However, this process converts harmful NH<sub>3</sub> into N<sub>2</sub> and water, thereby reducing environmental pollution and preventing ammonia emissions into the atmosphere. NH<sub>3</sub> electrooxidation can also be integrated with renewable energy sources, particularly where NH<sub>3</sub> is produced from renewable H<sub>2</sub>, creating a closed-loop sustainable process. Its applications include wastewater treatment and nitrogen removal from industrial effluents, with potential uses in H<sub>2</sub> production.

Briefly, NH<sub>3</sub> electrolysis is a process of dissociating the liquid NH<sub>3</sub> or ammonium in electrochemical cells. Fig. 3 illustrates the basic concept of NH<sub>3</sub> electrolysis. Unlike the photoelectrochemical water-splitting approach, NH<sub>3</sub> electrolysis is a process that is been conducted in the absence of light. This process begins with the direct supply of electricity from the power supply to the system. Typically, in an aqueous NH<sub>3</sub> electrolysis system, as the charges flow through the circuit, the anode electrode undergoes the oxidation of NH<sub>3</sub> to the nitrates compound which then further oxidizes to N<sub>2</sub> molecules. Concurrently, the produced electrons at the anode will be transferred to the cathode electrode for subsequent reduction of water molecules to the H<sub>2</sub> products.<sup>24</sup> On this side, the H<sub>2</sub> evolution reaction (HER) will take place by reducing the water molecules with a consumption of six electron species.

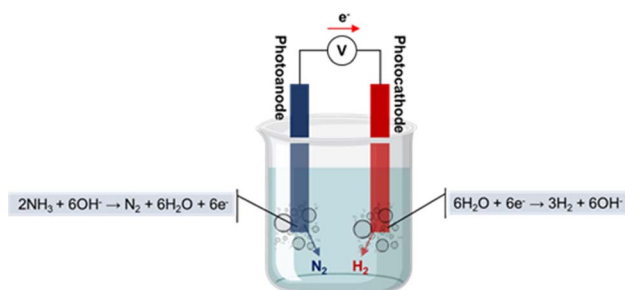
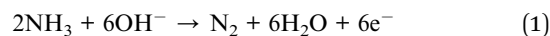
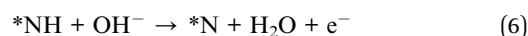
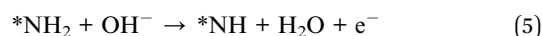
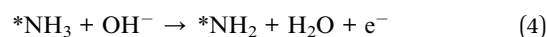


Fig. 3 Principle of electrolysis NH<sub>3</sub> in aqueous solution for H<sub>2</sub> production.

Moreover, the mechanism of NH<sub>3</sub> electrolysis can be described by the equations below:<sup>25</sup>



Adsorption of NH<sub>3</sub> onto the surface of the catalyst initiates the six-electron in AOR process as well as takes place in an alkaline environment. Significantly, the AOR is traversed *via* two discrete pathways (Fig. 4).<sup>26</sup> Oswin and Salomon introduced the O-S mechanism, a consistent dehydrogenation process, in 1963 as reported by Kim *et al.*<sup>27</sup> In this mechanism, \*NH<sub>3</sub> on the surface of catalyst undergoes sequential dehydrogenation by OH<sup>-</sup> to form \*N, which later combines to form N<sub>2</sub>. Thus, the O-S mechanism can be described as shown in eqn (3)–(7):



Subsequently to this research, the O-S mechanism was later fine-tuned by Mauerer and Gerischer. Contradict, those

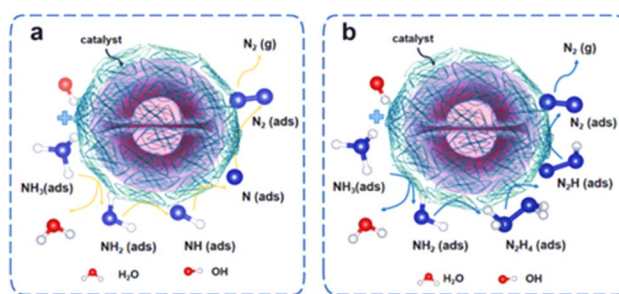
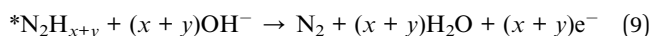
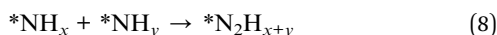


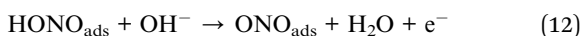
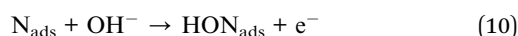
Fig. 4 Oxidation of NH<sub>3</sub> by O-S (a) and G-M (b) mechanism. Reproduced from ref. 26 with permission from Elsevier, copyright 2024.

## Review

researchers proposed that the G–M mechanism in the AOR involves the recombination of  $*N_xH_y$  species as well as  $OH^-$  dehydrogenation.<sup>28</sup> The G–M mechanism is represented by eqn (8) and (9) below, where  $x = 1$  or 2, and  $y = 1$  or 2.



The dehydrogenated  $*NH$  and  $*NH_2$  were combined to form  $*N_2H_{x+y}$ . Subsequent dehydrogenation of  $*N_2H_{x+y}$  leads to the formation of  $N_2$ . In both major mechanisms, the rate-determining step is the dimerization of  $*NH_x$  and  $*N$  ( $N_{ads}$ ), which significantly limits the production of  $N_2$  from  $NH_3$  oxidation. However,  $N_{ads}$  can be further oxidized by  $OH^-$  to generate N–O intermediates, which then form nitrite and nitrate.



Driven by the catalyst, the  $OH_{ads}$  produced in the electrolyte possess high bonding energies, which halts the dimerization process of  $N_{ads}$ , leading to their further oxidation to  $NO_2^-$  and  $NO_3^-$ .<sup>26</sup> During this process, under the influence of  $OH^-$  in the electrolyte, the  $N_{ads}$  adsorbed on the catalyst surface are gradually hydroxylated to form species such as  $HON_{ads}$ ,  $ONO_{ads}$ , etc., which are then converted to  $ONoads$  before being smoothly oxidized to  $NO_2^-$  and  $NO_3^-$ . For example, the strongly adsorbed  $N_{ads}$  hinder the further adsorption of  $NH_x$ , resulting in a poor AOR reaction rate. A catalyst, such as CuNi, is expected to exhibit favorable AOR activity for  $N_2$  production only if it possesses appropriate adsorption bonding energy for each intermediate (Fig. 5a and b).<sup>29</sup>

Most research supports the idea that intermediates recombine in the AOR. Additionally, analyses like DEMS and SERS have indicated that  $N_2$  cannot be generated into fully dehydrogenated  $*N$ ; instead, it acts merely as a poisoning species. Several investigations have linked AOR intermediates to negative health effects, which has sparked discussion over AOR intermediates like  $*N_x$ ,  $*N_xH_y$ , and  $*NO_x$ . Accordingly, the key to getting high AOR activity is minimizing poisoning by  $N_x$ ,  $NO_x$ , and  $N_xH_y$  and improving the recombination of  $N_xH_y$  species.

A straightforward and effective defect-engineering strategy offers a robust approach for AOR mechanistic studies, where oxygen vacancies (Vo) are found to effectively modulate the electronic properties of surface CuO and enhance the binding strength of reaction intermediates.<sup>30</sup> Conventional Pt-based electrocatalysts are generally believed to follow the G–M mechanism because the key intermediate of  $N_2H_4$  was detected. However, the O–S mechanism reaction route *via*



Fig. 5 Ammonia oxidation for the preparation of (a)  $NO_2^-$  and (b)  $NO_3^-$  mechanism. Reproduced from ref. 26 with permission from Elsevier, copyright 2024.

dehydrogenation of  $NH_3$  to N and N–N coupling is applied to the rich Vo–CuO. Based on the free energy pathway of the AOR process *via* DFT simulations, the  $NH_3$  adsorption process is energetically unfavourable on the Vo-free CuO surface. The free energy changes of the three dehydrogenation steps are all uphill and higher than 1.4 eV due to weak adsorption towards  $*NH_x$  species, with the largest free energy change being 1.75 eV, indicating inferior AOR activity (Fig. 6A).<sup>30</sup> However, after introducing the Vo, the free energy of each step decreases by 0.34, 1.84, 2.84, and 2.64 eV, respectively. Additionally, the electronic structures of Cu atoms on the different surface CuO showed that the local density of states of surface Cu atoms move significantly upward towards the Fermi level after introducing Vo, indicating stronger adsorption strength towards the adsorbates. Therefore, the presence of the Vo is beneficial to efficient  $NH_3$  oxidation by stabilizing reaction intermediates. Similarly, Zhang *et al.* claimed that the AOR pathways follow the N + N mechanism containing the  $N_2H_3$  and  $N_2H_4$  intermediate by using TiO–Vo.<sup>32</sup> The introduction of Vo made the  $N_2$  desorption a spontaneous exoergic process, which was a good solution to the most critical catalyst poisoning problem in the AOR process.

Differently, Yang *et al.* reported that  $CeO_2$  with Vo species are the active species in the  $CeO_x/Y$  electrode during ammonia electrolysis and follow the G–M mechanism involving the  $N_2H_4$  intermediates (Fig. 6B).<sup>31</sup> Generally, the dehydrogenation of  $*NH_3$  to  $*NH_2$  is usually the rate-determining step for AOR over metal oxides. In this study, the energy barrier for the conversion of  $*NH_3$  to  $*NH_2$  on  $CeO_2$  is 2.13 eV, whereas on  $CeO_2$ –Vo it is only  $-0.26$  eV, indicating that  $NH_3$  is readily deprotonated. This

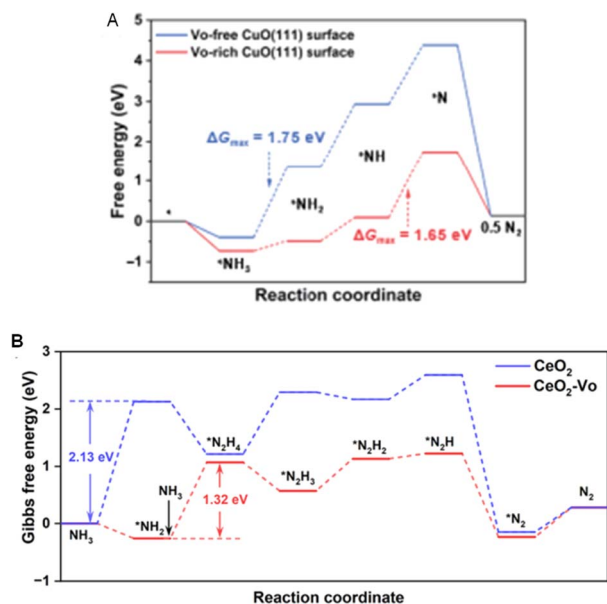


Fig. 6 Free energy diagrams of NH<sub>3</sub> oxidation into N<sub>2</sub> on the (A) Vo-rich and Vo-free CuO via O–S mechanism. Reproduced from ref. 30 with permission from Springer, copyright 2022 and (B) CeO<sub>2</sub> and CeO<sub>2</sub>-Vo follow the G–M mechanism. Reproduced from ref. 31 with permission from ACS Publications, copyright 2024.

shows that the NH<sub>3</sub> oxidation process is energetically unfavourable on the CeO<sub>2</sub> surface, but the presence of Vo in CeO<sub>2</sub> significantly reduces the energy barrier for  $\text{*NH}_3$  to  $\text{*NH}_2$ , aligning with the enhanced AOR activity of CeO<sub>2</sub>-Vo. When NH<sub>3</sub> adsorbs on Vo sites, one elongated N–H bond points toward a neighboring H atom. The elongation of the N–H bond and the attraction of neighboring O atoms facilitate H transfer. Therefore, it can be concluded that the presence of Vo in CeO<sub>2</sub> not only enhances NH<sub>3</sub> adsorption but also lowers the energy barrier for NH<sub>3</sub> dehydrogenation. This contributes to the increased activity of NH<sub>3</sub> electrolysis following the G–M mechanism.

Achieving high NH<sub>3</sub> electrolysis performance is the main goal for all researchers. Similar to the water-splitting reaction, optimizing the electrochemical cell of NH<sub>3</sub> electrolysis should take into consideration the type, pH and concentration of the electrolyte, and the electrode materials. Frankly speaking, ammonium-based electrolytes such as NH<sub>4</sub>Cl, NH<sub>4</sub>Br, NH<sub>4</sub>I, NH<sub>4</sub>NO<sub>3</sub>, and NH<sub>4</sub>PF<sub>6</sub> are the most suitable electrolytes for NH<sub>3</sub> electrolysis since this process involves the reduction of ammonium species to generate H<sub>2</sub> gas.<sup>33</sup> In addition, the influence of pH on AOR is something that needs to be taken into consideration. Typically, the current density measurement in the AOR rises steadily as the pH goes up, while the starting potential of the anode decreases in line with pH increments. In the study of AOR, alkaline-based electrolytes remain the most commonly used because NH<sub>3</sub> can stay in its molecular form more effectively in these conditions, generally leading to better AOR performance.<sup>26</sup> On the other hand, NH<sub>3</sub> indirect oxidation in acidic media is a very slow process because NH<sub>4</sub><sup>+</sup> is pushed away from the electrodes in acidic ions. Moreover, the oxidation of

NH<sub>3</sub> in low pH media often made the anode material susceptible to undesirable corrosion which greatly hampers the AOR process. However, an area of potential interest for AOR is the use of non-aqueous electrolytes, which can eliminate undesirable water oxidation side reactions, narrow AOR potential apertures, and the formation of by-products like nitrates. Therefore, regulating the pH of an AOR system logically is a crucial factor that merits investigation.

Moreover, the concentration of NH<sub>3</sub> in the electrolyte solution also greatly influences the electrolysis performance. Utilising an electrolyte containing a high concentration of NH<sub>3</sub> in this instance can enhance the interaction between NH<sub>3</sub> and the catalyst, resulting in substantial production of H<sub>2</sub>. In a recent study, Tran *et al.* observed an enhancement in faradaic efficiency along with an increase in NH<sub>3</sub> concentration.<sup>34</sup> Similarly, Jo *et al.* also found that the AOR performance is directly proportional to the initial concentration of NH<sub>3</sub> which concluded that a high concentration of NH<sub>3</sub> is favorable for high H<sub>2</sub> production.<sup>35</sup> Despite these circumstances, the employment of a high concentration of NH<sub>3</sub> in the electrolysis process might upsurge the overall process cost and unsuitable for large-scale implementation. Therefore, optimization of economic cost and electrolysis performance are substantially important for the systematic design of NH<sub>3</sub> electrolysis systems.

Furthermore, it has been validated that the electrochemical reaction occurring at the anodic electrode constitutes the rate-limiting step in the NH<sub>3</sub>-to-H<sub>2</sub> conversion process. Hence, the selection of an appropriate anodic electrode exhibiting outstanding physicochemical and electrical characteristics is imperative. Notably, there exist specific prerequisites to be fulfilled when opting for the anodic material. Primarily, the material must possess elevated physicochemical stability, ensuring minimal or negligible degradation throughout the electrolysis procedure, thereby preserving its original attributes. Additionally, the stability of the anodic material plays a pivotal role in preventing undesired side reactions that could pose environmental hazards and compromise the efficacy of the anodic electrode in the AOR.<sup>36</sup> Moreover, since the anode electrode undergoes an oxidation reaction, the anode must demonstrate exceptional corrosion resistance to ensure an efficient AOR process. Long-term stability of the anodic material during electrolysis is essential for its viability in commercial applications, particularly in industrial processes. Specifically, a high surface area of anode material is desired for the AOR process. The high surface area with exceptional active sites can enhance the surface electrode–electrolyte interface and accelerate the AOR process, ultimately leading to high production of H<sub>2</sub>.<sup>26</sup> Electronic properties are of paramount importance, with the anodic material requiring excellent electron and ion transport capabilities to sustain high current densities and minimize energy losses during the process. Lastly, to ensure heightened and efficient AOR activity, the anodic material should exhibit low overpotential values and high selectivity towards N<sub>2</sub> production over NO<sub>x</sub> compounds.<sup>34</sup>

Over the years, due to the extraordinary properties of Pt, such as a lower  $\text{*N}$  affinity than other noble metals and a superior dehydrogenation capacity of NH<sub>x</sub> in comparison to non-noble

metals, Pt-based materials have garnered considerable interest in the AOR study. This has resulted in superior AOR performance. Nevertheless, the high cost of utilizing Pt has restricted its practical applications. On the other hand, even though non-noble metal demonstrated low AOR efficiency compared to noble metal, its overall efficiency can still be improved by further modification. Therefore, single-atom catalysts and transition-metal-based catalysts have been widely employed for  $\text{NH}_3$  electrolysis studies.

## Electrocatalysts for AOR in $\text{NH}_3$ -to- $\text{H}_2$ conversion

The performance of two classes of AOR catalysts is the primary focus of this section: (1) transition metal-based electrocatalysts and (2) single-atom (SACs) electrocatalysts. Because of their high selectivity, stability, and catalytic activity, SACs electrocatalysts have emerged as promising candidates for  $\text{NH}_3$  oxidation. Dispersed on a support material are isolated metal atoms that constitute these catalysts. SACs are distinguished by their electronic and geometric configurations, which enable them to facilitate charge transfer with high efficiency and furnish active sites for the oxidation of  $\text{NH}_3$ . Recent research has demonstrated the excellent performance of SACs in  $\text{NH}_3$  electrooxidation, offering high conversion efficiency and superior selectivity for  $\text{H}_2$  production. Additionally, SACs exhibit remarkable stability, making them attractive candidates for practical applications.

Transition metal-based electrocatalysts have also shown promising performance in  $\text{NH}_3$  electrooxidation. These electrocatalysts typically consist of transition metal nanoparticles or alloys supported on conductive substrates. Transition metals such as nickel (Ni), cobalt (Co), and copper (Cu) have been extensively studied for  $\text{NH}_3$  oxidation due to their high catalytic activity and stability. Transition metal-based electrocatalysts offer several advantages, including tunable electronic properties and high surface area, which enhance catalytic activity and facilitate  $\text{NH}_3$  oxidation.<sup>6</sup> Moreover, the abundance and low cost of transition metals make them attractive candidates for large-scale  $\text{H}_2$  production *via* AOR. Table 1 shows the summary of single atoms catalysts and transition metal-based electrocatalysts for  $\text{H}_2$  production *via* AOR.

### Single-atom electrocatalysts

Single-atom catalysts, which comprise an isolated active site composed of a single metal atom, have made significant strides in recent years and have been recognized as the most promising electrocatalysts.<sup>58,59</sup> In contrast to conventional nanoparticle catalysts, the utilization of metal sites in an isolated dispersion maximizes atom utilization. This not only results in a substantial cost reduction but also imparts exceptional catalytic activity and selectivity. The study conducted by Akagi *et al.* examines the potential of anodic catalysts such as Pt, Ru, Ir, Co, Ni, Ta, Fe, and Ti in the electrolysis of liquid  $\text{NH}_3$ .<sup>33</sup> The current densities were as follows:  $\text{Ru} > \text{Ni} > \text{Co} > \text{Ir} > \text{Pt} > \text{Fe}$  at 0.3 V *versus*  $\text{H}_2/\text{NH}_3$  (Fig. 7A). The AOR reaction on Ti, Ta, Fe, and Co is constrained

Table 1 Single atoms catalyst and transition metal-based electrocatalysts for  $\text{H}_2$  production *via* AOR

| Catalyst   | Current density ( $\text{mA cm}^{-2}$ ) | Onset potential ( $V_{\text{RHE}}$ ) | Ref. |
|--|---|--------------------------------------|------|
| Ni films   | 0.45                                    | 0.3                                  | 33   |
| Pt nanoparticle  | 1.45                                    | 0.9                                  | 24   |
| Pt nanosphere  | 2.6                                     | —                                    | 37   |
| Pt/Rh  | 2.5                                     | 0.53                                 | 38   |
| Pt/NC  | 2.4                                     | 0.1                                  | 39   |
| PtIrCu nanodendrites   | 122.9 $\text{A g}^{-1}$                 | 0.35                                 | 40   |
| PtIrCu nanoframe   | —                                       | 0.33                                 | 41   |
| PtRu/C   | 0.1                                     | 0.2                                  | 42   |
| PtIrZn   | 0.0043                                  | 0.3                                  | 43   |
| Pt/NiO   | 0.24                                    | -0.48                                | 44   |
| Pt/TiO <sub>2</sub> /S-OLCN  | 0.28                                    | -0.501                               | 45   |
| Pt/SnO <sub>2</sub> /C   | —                                       | 0.07                                 | 14   |
| TM <sub>2</sub> @g-CN  | —                                       | -0.48                                | 46   |
| RuO <sub>2</sub> -ZnO/Al <sub>2</sub> O <sub>3</sub>   | 0.74                                    | 0.2                                  | 47   |
| TiO <sub>2</sub> nanofibers  | 0.06                                    | 0.4                                  | 32   |
| NiO-TiO <sub>2</sub>   | 2.93                                    | 1.24                                 | 10   |
| Co/Ni-C  | 2.0                                     | 0.45                                 | 48   |
| NiCO <sub>2</sub> N nanoneedle   | 10                                      | 0.71                                 | 21   |
| NiCO <sub>2</sub> N nanosheets   | 10                                      | 0.55                                 | 15   |
| NiCuBO/NF  | 25                                      | 1.301                                | 49   |
| B-NiFe-LDH/NF  | 100                                     | 1.481                                | 50   |
| Ni(OH) <sub>2</sub> -Cu <sub>2</sub> O@CuO   | 10                                      | 0.47                                 | 51   |
| Ni <sub>1-x</sub> Cu <sub>x</sub> OOH  | 35                                      | 0.28                                 | 52   |
| Cu <sub>2</sub> O/NF   | 4.6                                     | 0.55                                 | 53   |
| Ni <sub>3</sub> S <sub>4</sub> @NiCo <sub>2</sub> O <sub>4</sub> /NF                                       | 50                                      | 0.63                                 | 54   |
| LaNi <sub>0.5</sub> Cu <sub>0.5</sub> O <sub>3-<math>\delta</math></sub>                                   | 10                                      | 0.55                                 | 55   |
| La <sub>1-y</sub> Ni <sub>0.6</sub> Cu <sub>0.4-x</sub> Fe <sub>x</sub> O <sub>3-<math>\delta</math></sub> | 50                                      | 0.55                                 | 56   |
| La <sub>0.5</sub> Sr <sub>1.5</sub> Ni <sub>0.9</sub> Cu <sub>0.1</sub> O <sub>4-<math>\delta</math></sub> | 13.4                                    | 0.53                                 | 57   |

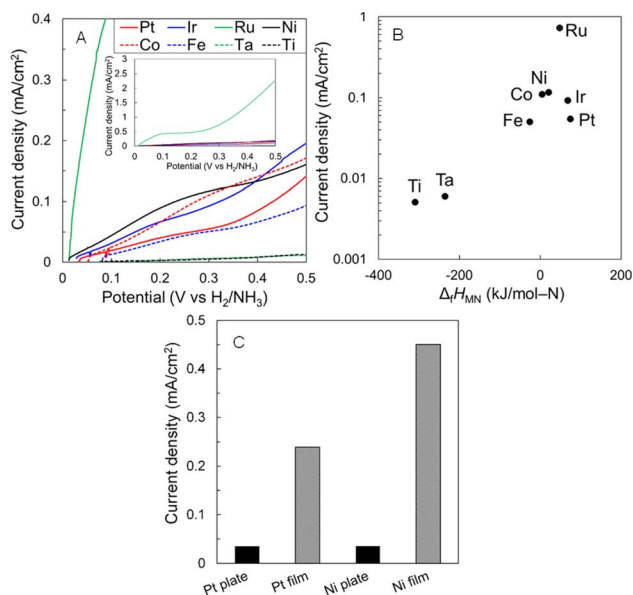


Fig. 7 (A) LSV curves at  $10 \text{ mV s}^{-1}$ , (B) volcano plot of current density at 0.3 V *vs.*  $\text{H}_2/\text{NH}_3$  as a function of metal nitride formation enthalpy ( $\Delta_f H_{\text{MN}}$  ( $\text{kJ mol}^{-1} \text{N}^{-1}$ )) of various metal plates, and (C) current density for Pt and Ni plates and films for anodic reaction in liquid  $\text{NH}_3$  with 0.5 M  $\text{KNH}_2$ . Reproduced from ref. 33 with permission from Elsevier, copyright 2022.

by nitrogen desorption, as these elements possess a low metal nitride formation enthalpy ( $\Delta_f H_{MN}$ ) by their high affinity for nitrogen. However, since Ir and Pt have a greater  $\Delta_f H_{MN}$ ,  $H_2$  scission or  $NH_2$ -adsorption from  $NH_x$  to form N atoms restricts the rate at which they occur. At the apex of the volcano correlation, Ru exhibiting a moderate  $\Delta_f H_{MN}$  was identified, indicating the greatest catalytic activity<sup>33</sup> (Fig. 7B). Additionally, the authors investigated the impact of Pt and Ni electrode surface configurations, such as plates and films. The current density of the sputtered Pt and Ni films, which possessed a columnar structure and an uneven surface, was observed to be seven and thirteen times greater than that of the Pt and Ni plates, respectively. The sputtered Ni film demonstrated an anodic current density of  $0.45 \text{ mA cm}^{-2}$  at an anodic potential of  $0.3 \text{ V}$  versus  $H_2/NH_3$  (ref. 33) (Fig. 7C).

The Pt catalyst is the most frequently utilized noble metal catalyst in AOR research.<sup>24</sup> The selection of an ideal electrolyte is critical in optimizing the functionality of electrocatalysts in AOR. In addition to providing the electrolyte with the ions required for the electrochemical reaction, it also affects the stability of the catalyst, the rate of the reaction, and the selectivity of the product. In general, the majority of researchers employed non-aqueous electrolytes; nevertheless, this approach resulted in a rapid decrease in current due to the electrode becoming contaminated with nitride that formed on the anode surface. The incorporation of methanol into the  $PF_6^-$ -DMF (non-aqueous electrolyte), as suggested by Yang *et al.*, significantly improves the electrochemical characteristics of the system, including  $NH_3$  electrolysis stability reduced polarization resistance, and high current density.<sup>41</sup> The  $NH_3$  electrolysis is conducted for 2 hours in the absence of methanol, during which the current density stabilizes at approximately  $0.24 \text{ mA cm}^{-2}$ . The abrupt increase in current density occurs when 5 wt% methanol is added to the  $KPF_6^-$ -DMF non-aqueous electrolyte. The stabilized current density of  $1.45 \text{ mA cm}^{-2}$  is exactly six times that of the  $KPF_6^-$ -DMF non-aqueous electrolyte when methanol is not present. Methanol diminishes the intensity of the adsorption of  $N^*$  species onto the Pt electrode surface, thereby impeding the formation of a nitridation layer.<sup>60</sup>

In recent times, considerable effort has been devoted to modifying the surface orientation and morphologies of Pt particles in an attempt to expose a greater number of active sites. As an illustration, Liu *et al.* investigated different morphologies of Pt architectures including flower, sheet, cauliflower-like shapes, and prickly spheres, to demonstrate that the AOR activity is significantly influenced by the Pt surface morphology. Due to better diffusion control, prickly nanospheres had a current density of  $2.6 \text{ mA cm}^{-2}$  and better AOR performance than smooth nanoparticles<sup>37</sup> (Fig. 8A). Both the high SSA and the high electrocatalytic activity per unit SSA of smooth, spherical Pt particles explain why they are so much more active as electrocatalysts than hierarchical Pt particles<sup>37</sup> (Fig. 8B). Because of the high electrochemically accessible area of the electrocatalyst and the increase of the interaction with water, nitrogen-doped carbon ( $2.4 \text{ mA cm}^{-2}$ ) and Rh surface entities ( $2.5 \text{ mA cm}^{-2}$ ) can improve the AOR on Pt nanoparticles.<sup>38,39</sup> An analogous result was observed when PtIrCu

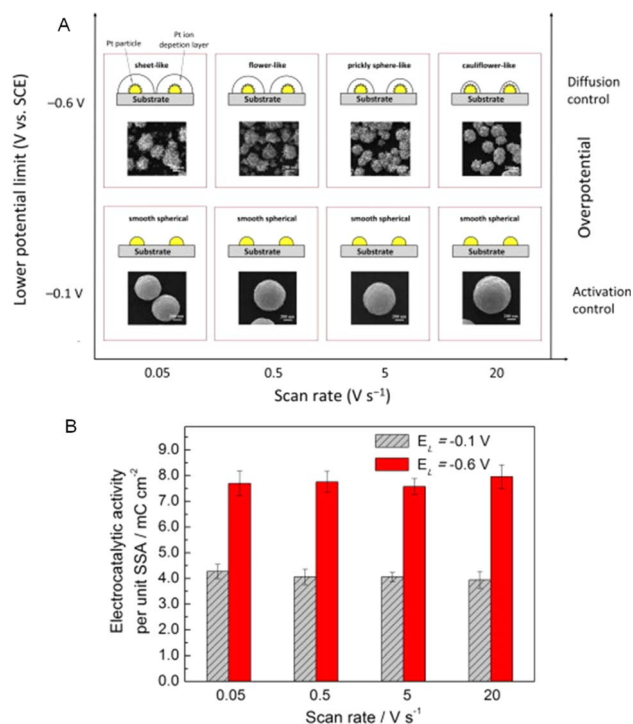


Fig. 8 (A) Schematic representation of a two-dimensional map illustrating how the voltage difference and scan rate affect the particle morphologies; and (B) Pt particles with varied morphologies and EL values of  $-0.1 \text{ V}$  and  $-0.6 \text{ V}$  have varying electrocatalytic activity per unit SSA. Reproduced from ref. 37 with permission from Elsevier, copyright 2013.

hyperbranched concave octahedral nanodendrites improved the electronic effect, exhibiting the highest current density ( $122.9 \text{ A g}^{-1}$ ) and the onset potential ( $0.35 \text{ V vs. RHE}$ ).<sup>40</sup> The exceptional performance of PtIrCu can also be ascribed to the presence of profuse suspended bonds on the high-index facets  $\{553\}$ ,  $\{331\}$ , and  $\{221\}$ , which readily interact with  $NH_3$  and promote  $NH_3$  oxidation. In a separate study, Yang *et al.* documented the characteristics of a rhombic dodecahedron nano-frame composed of PtIrCu featuring high-index faceted hyperbranched nanodendrites (RDNF-HNDs). These nanodendrites exhibited a high mass activity of  $26.1 \text{ A g}_{PtIr}^{-1}$  at  $0.50 \text{ V}$ , which is 7.5 times greater than the mass activity of commercial Pt/C in the AOR 36 and 140 mV lower than RHE.

AOR is influenced by the surface orientation of Pt nanocrystals. AOR occurs mostly on the Pt (100) crystalline plane rather than on the Pt (111) and (110) planes.<sup>14,28,61,62</sup> In contrast to low-index surfaces, high-index crystal surfaces are adorned with an abundance of suspended bonds that facilitate reaction with reactants and thereby augment catalytic activity.<sup>63,64</sup> For AOR, Vidal-Iglesias *et al.* utilized PtMe (Me: Pd, Rh, Ir, Ru) with a particular orientation of Pt (1 0 0) nanoparticles. Out of all the bimetallic samples that were examined, only PtIr and PtRh nanoparticles exhibited an increase in the oxidation density current at low potentials, in contrast to the behavior observed in pure Pt nanoparticles synthesized using the identical technique. PtIr and PtRh nanoparticles, which are preferentially

oriented with Pt (100), exhibit greater current densities than polycrystalline Pt nanoparticles. This is because AOR is more sensitive to the presence of square-symmetrical surface sites. On roughened surfaces, however, an increased proportion of exposed Pt(311) planes can substantially increase (by up to 550%) the activity of Pt toward AOR.<sup>65</sup>

Furthermore, one way to manipulate electrical structures is by alloying Pt with other metals.<sup>66</sup> Pt is alloyed with noble metals like PtPd, PtRh, PtRu, and PtIr to increase the AOR's catalytic activity and lower the onset potential by lowering the dehydrogenation reaction's dissociation energy.<sup>42,67–70</sup> The addition of Ir to Pt, for instance, can substantially decrease the activation energy of NH<sub>3</sub> on Pt, thereby decreasing the AOR overpotential.<sup>71</sup> On the other hand, according to the free energy calculations, the onset potential for AOR is lower on Ir compared to Pt. Ir-coated Pt nanocubes, according to Siddharth *et al.*, are the surface-engineered model catalysts for AOR.<sup>9</sup> A comparison of adsorption energies revealed that reaction intermediates, specifically \*NH<sub>3</sub>, bind more strongly to Ir-decorated Pt (100) with a binding energy of  $-1.68$  eV than to Pt (100) with a binding energy of  $-1.44$  eV. This stronger adsorption on Ir-decorated Pt (100) suggests that the catalyst could enhance AOR kinetics. Fig. 9A shows the Gibbs free energy curves for AOR pathways on Pt(100) and Ir-decorated Pt(100). Among the three pathways (N<sub>2</sub>H<sub>2</sub>, N<sub>2</sub>H<sub>3</sub> and N<sub>2</sub>H<sub>4</sub>), a N<sub>2</sub>H<sub>3</sub> pathway is the most favourable one, where the \*NH<sub>2</sub>-to-\*NH is the rate-determining step with the energy barrier of 0.96 eV for Pt (100).<sup>9</sup> Interestingly, a reduced energy barrier of 0.74 eV for \*NH<sub>2</sub>-to-\*NH step is observed for Ir-decorated Pt(100). They also investigated the optimized structure of AOR intermediates and discovered that there are five optimized structures for favorable N<sub>2</sub>H<sub>3</sub> pathways on Ir-decorated Pt(100). Comparing the

energy levels in Fig. 9B reveals that a greater binding to the chemical intermediates is facilitated by the surface Ir.<sup>9</sup> Simulation results show that Ir-decorated Pt NCS/C promote reaction intermediate adsorption and lower the energy barrier during the potential determining phase, increasing their activity.

In addition, adding 3D transition metals like PtIrZn and PtIrNi to PtIr alloy increased AOR activity.<sup>43,72</sup> An instance of this can be seen in the PtIrZn electrode, which exhibits a low onset potential of 0.30 V relative to RHE and a high exchange current density of 0.0043 mA cm<sup>-2</sup>. This indicates that in contrast to the nanostructuring of PtIr, the most probable source is the introduction of Zn. H<sub>2</sub> electrochemistry takes place on Pt-based electrodes between 0 and 0.40 V; therefore, dissociative adsorption of NH<sub>3</sub> ought to compete with H<sub>2</sub> adsorption. The inhibition of competitive H<sub>2</sub> adsorption would be advantageous. This may be accomplished by introducing Zn with a high H<sub>2</sub> overpotential into PtIr.

For PtIrNi, the catalyst showed significantly enhanced AOR activity with a reduced onset potential of approximately 0.40 V, compared to the binary PtIr and bare Pt catalysts. This improvement can be explained by the d-band model. The electronic structure analysis revealed that Ir atoms on the surface have a higher d-band center relative to Pt atoms ( $-1.97$  vs.  $-2.25$  eV), resulting in fewer occupied antibonding states and stronger adsorption energies for \*NH<sup>72</sup> (Fig. 10A). Adding Ni to the surface further shifts the d-orbital density of states up in energy ( $-1.97$  to  $-1.87$  eV), strengthening the adsorption of \*NH intermediates and enhancing AOR activity. This group orbital model theoretically supports the promotional role of Ni in PtIr alloys for improved AOR performance. The Gibbs free energy pathways also supported that with the addition of a Ni atom to the Pt<sub>3</sub>Ir(100) surface, the dehydrogenation of \*NH<sub>2</sub> to \*NH becomes exergonic at 0.3 V vs. RHE which lowering the thermodynamic barrier in the dehydrogenation process<sup>72</sup> (Fig. 10B).

In addition to promoting alloy formation, Pt-supported metal oxide at the nanoscale can also accelerate the AOR reaction. Ntais *et al.* accomplished the synthesis of platinum nanoparticles that were backed by NiO, MnO<sub>2</sub>, and carbon black.<sup>44</sup> As compared to Hg/HgO, Pt/NiO exhibited the greatest current density (0.24 mA cm<sup>-2</sup>) and the least onset potential for AOR ( $-0.48$  V). Similarly, Pt supported on TiO<sub>2</sub> nanoparticles and embellished with sulfur-doped onion-like carbon nanoparticles (S-OLCNs) exhibited superior resistance to charge transfer and enhanced long-term stability.<sup>45</sup> Pt/TiO<sub>2</sub>/S-OLCN demonstrated a current density of 0.28 mA cm<sup>-2</sup>, which is greater than that of commercial Pt/C. The enhanced catalytic performance of the Pt/TiO<sub>2</sub>/S-OLCN electrocatalyst can be attributed to the cohesive metal-support interface formed by the S-OLCN-TiO<sub>2</sub> composite support material and Pt nanoparticles. Additionally, this may be the result of the "spillover" phenomenon, in which intermediates adsorbed on Pt sites migrate to adjacent Ti-OH species to aid in the acceleration of oxidation. TiO helps keep the Pt catalyst from becoming inactivated by N<sub>2</sub> intermediates (Pt-N<sub>ads</sub>), which are harmful to the Pt that is created during the AOR. In addition, the Pt/TiO<sub>2</sub>/S-OLCN catalyst will be more able to catalyse the creation of AOR because the Pt NPs and the S groups in the onion structure



Fig. 9 (A) Gibbs free energy curves for AOR pathways on Pt(100) and Ir-decorated Pt(100) and (B) optimized structures (top and side views) of reaction intermediates using the N<sub>2</sub>H<sub>3</sub> route during AOR on Ir-decorated Pt(100). Color code: Ir, pink; Pt, dark blue; H, white; N, blue. Reproduced from ref. 9 with permission from Springer, copyright 2020.

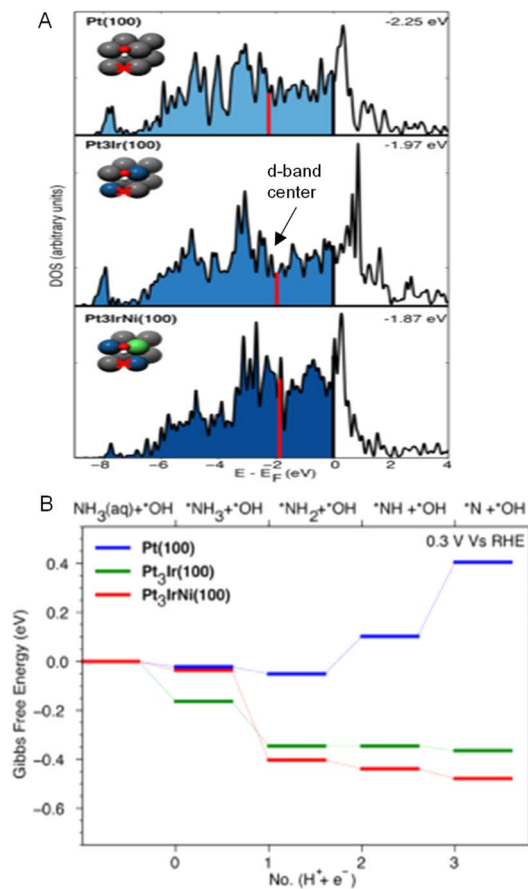


Fig. 10 (A) Group d-orbital density of states projected onto the bridge site of model systems and (B) free-energy pathway *via* constant-potential DFT calculations for initial ammonia dehydrogenation steps at 0.3 V vs. RHE on Pt(100), Pt<sub>3</sub>Ir(100), Pt<sub>3</sub>IrNi(100). Reproduced from ref. 72 with permission from ACS Publications, copyright 2020.

have robust electron transfer connectivity, which will change the surface's electrical state. Lastly, Barbosa *et al.* reported that PtSnO<sub>2</sub> nanoparticles with a preferential (100) orientation significantly decreased the onset potential for the AOR by approximately 70 mV.<sup>14</sup> The high catalytic activity of these materials is attributed to the Pt (100) orientation, which exhibits a higher tolerance for poisoning intermediates like adsorbed nitrogen species (N<sub>ads</sub>). Additionally, the presence of SnO<sub>2</sub> helps prevent the deactivation of the Pt surface caused by intermediates formed during the AOR.

Recently, Zhong *et al.* conducted a study on a series of transition metal atoms anchored at a g-CN monolayer (TM<sub>2</sub>@g-CN), including Fe, Co, Ni, Ru, Rh, Pd, Os, Ir, and Pt, to identify high-performance AOR electrocatalysts.<sup>46</sup> Compared with bulk Pt, the interaction between metal and support on the TM<sub>2</sub>@g-CN catalyst leads to a positive charge on the metal atoms, making their corresponding d orbitals easier to polarize and more effective at adsorbing NH<sub>3</sub> (ref. 46) (Fig. 11A). This interaction also accelerates the coupling of dinitrogen, reducing the onset potential of NH<sub>3</sub> oxidation to 0.48–0.52 eV, compared to the experimentally measured onset potential of 0.62 eV for the Pt (100) surface, without producing surface-poisonous nitrogen. Among all TM<sub>2</sub>@g-CN electrocatalysts, Fe, Co, Ru, Rh, and Ir



Fig. 11 (A) Adsorption energy of transition metal atoms anchored at a g-CN monolayer (TM<sub>2</sub>@g-CN) and (B) the scaling relationship between d band center (ε<sub>d</sub>) and the limiting potential (U<sub>L</sub>). Reproduced from ref. 46 with permission from Elsevier, copyright 2023.

anchored in the g-CN monolayer shows the most promise as AOR catalysts due to their low limiting potentials of -0.47, -0.5, -0.48, -0.52, and -0.48 V, respectively. Furthermore, the catalytic performance of these TM<sub>2</sub>@g-CN candidates strongly correlate with the d band center (ε<sub>d</sub>) of the TM atoms, which is beneficial for designing promising AOR catalysts. When the ε<sub>d</sub> shifts closer to the Fermi energy level, the limiting potential (U<sub>L</sub>) value becomes less negative, indicating increased activity<sup>46</sup> (Fig. 11B). Therefore, the ε<sub>d</sub> can directly predict AOR activity, and a downshift in the metal ε<sub>d</sub> helps maintain long-lasting electrocatalytic activity.

Based on the activation energy barrier, the dimerization of NH<sub>2</sub> in Ir<sub>2</sub>@g-CN is more favorable than in other metals, with an activation energy of 0.93 eV. The activation energies for the other four TM<sub>2</sub>@g-CN catalysts are 2.17, 1.76, 3.3, and 1.59 eV, all higher than the activation energy for the Pt (111) surface, which is 1.07 eV. Referring to the adsorption and activation energy, the mechanism proposed by G-M is kinetically preferred. This mechanism involves N-N bond formation *via* hydrogenated NH<sub>x</sub> species rather than N adatoms because the strong adsorption energy of NH<sub>2</sub> on the TM<sub>2</sub>@g-CN monolayer requires a large potential for NH<sub>2</sub> deprotonation into NH. Therefore, the N + N mechanism is not considered in this study.

In summary, recent research focuses on optimizing catalyst materials, morphologies, and surface orientations to enhance AOR performance, with a particular emphasis on single-atom catalysts and alloying strategies.

### Transition metal-based electrocatalysts

Active catalysts in AOR have been regarded as Pt and Pt-based noble metals due to their high  $N_2$  selectivity and low overpotential; nevertheless, their substantial expenses and vulnerability to deactivation have demonstrated themselves to be formidable obstacles. As an alternative to platinum-based electrocatalysts, non-noble metal-based electrocatalysts have been suggested recently. Non-noble metal catalysts, particularly transition metals (e.g., Ni-based compounds, CuO, Ni-Co bimetallic and Ni-Cu), are of interest in AOR for electrolytic  $H_2$  production and effluent cleanup.<sup>73</sup> After conducting a large number of theoretical calculations and practical investigations, it was shown that Ni possesses the highest HER exchange current density and the lowest free energy of  $H_2$  adsorption ( $*GH$ ) among a wide variety of nonprecious metals. Based on these findings, it appears that Ni could be a potential candidate for significantly increasing the intrinsic activity of HER. On the other hand, Yao *et al.* found that pure nickel had a low amount of AOR activity. This was because pure nickel had a high electrode consumption at the voltage that was required for  $NH_3$  oxidation.<sup>74</sup> It is not possible for NiO to effectively oxidize  $NH_3$  because the negative charge on the cation vacancies causes the generation of reverse electrons, which speeds up the deactivation of the anion.

In a recent study, Almomani *et al.* established that the addition of  $TiO_2$  to a Ni-based electrode substantially improves its efficacy for AOR.<sup>10</sup> The redox potential of Ni(II)/Ni(III) increased from +0.65 to 1.24 V as a result of the pretreatment technique for NiO nanocatalyst. This is in contrast to the redox potential of HgO/Hg, which remained unchanged. The  $NH_3$  oxidation potential is the component that is responsible for this increase. As an additional point of interest, it was observed that a potential of 1.24 V is sufficient to fully facilitate the transition of Ni(OH)<sub>2</sub> into NiOOH, which is a situation that encourages the oxidation of  $NH_3$ . In the interim, NiO- $TiO_2$ -treated nanopowders demonstrated a notable enhancement in their ability to achieve AOR. As the redox potential for the Ni(II)/Ni(III) reaction increased from +0.72 to 1.35 V, a strongly oxidising environment was formed. This resulted in a rise in the built-on Ni(OH)<sub>2</sub> layer, which in turn led to the oxidation of a bigger quantity of  $NH_3$ . In fact, metallic Ni and NiOOH are not catalytically active unless they are electrochemically converted to NiOOH at approximately 1.3 V vs. RHE. The dehydrogenation of  $NH_3$  begins with an electron-coupled proton transfer to NiOOH, resulting in a would-be reversible reduction of NiOOH to Ni(OH)<sub>2</sub>.<sup>75</sup> Huang *et al.* reported that Cu<sub>2</sub>O wire-in-Ni(OH)<sub>2</sub> plate passivated by a thin CuO surface (Ni(OH)<sub>2</sub>-Cu<sub>2</sub>O@CuO) achieves a stable current density as high as  $\sim 80$  mA cm<sup>-2</sup> for more than 30 h, demonstrating a much superior AOR performance than the previous works.<sup>51</sup> This novel wire-in-plate nanostructure, featuring intimate contact among Ni(OH)<sub>2</sub>, Cu<sub>2</sub>O, and CuO, develops dual interfaces of Ni(OH)<sub>2</sub>-Cu<sub>2</sub>O and Cu<sub>2</sub>O@CuO. These interfaces effectively protect Cu<sub>2</sub>O from oxidation and inhibit the dissociation of copper species into the electrolyte. In addition, after adding 1 M  $NH_3$  into the

electrolyte, a large current density of  $\sim 60$  mA cm<sup>-2</sup> was detected with an onset potential of 0.47 V vs. Hg/HgO for 10 mA cm<sup>-2</sup>.

Similarly, Xu *et al.* found that Cu effectively improve activity of Ni(OH)<sub>2</sub> for  $NH_3$  electrooxidation which mixed NiCu layered hydroxides achieve a current density of 35 mA cm<sup>-2</sup> at 0.55 V vs. Ag/AgCl and 0.28 V of onset potential at higher NaOH concentration, which is much higher than that of bare Ni(OH)<sub>2</sub> catalyst (5 mA cm<sup>-2</sup>).<sup>52</sup> This is attributed to the abundant active sites and the synergistic effect between Ni and Cu, likely due to the formation of Ni<sub>1-x</sub>Cu<sub>x</sub>OOH on the surface of the catalysts through the electrochemical activation of the mixture of Cu(OH)<sub>2</sub> and Ni(OH)<sub>2</sub>. Xu *et al.* also claimed that NiOOH is the actual active substance.<sup>76</sup> NiOOH is formed from  $\beta$ -Ni(OH)<sub>2</sub> via an electrochemical reaction in an alkaline solution to catalyze  $NH_3$  oxidation and then is reduced back to  $\beta$ -Ni(OH)<sub>2</sub> (eqn (15) and (16)). This study showed that without Ni element, the Cu catalyst was found to have negligible activity.



In details, Tsai *et al.* reported that Ni foam (NF) exhibited a redox couple of  $\alpha$ -Ni(OH)<sub>2</sub>(s)  $\leftrightarrow$   $\gamma$ -NiOOH(s) at 0.65 V and 0.38 V on the positive and negative scans.<sup>53</sup> However, an irreversible anodic peak at approximately 0.95 V (vs. Hg/HgO) was observed when the addition of Cu<sub>2</sub>O with different three morphologies of flower, particle, and sheet Cu<sub>2</sub>O. This result indicated that the transformation of  $\beta$ -Ni(OH)<sub>2</sub>(s) to  $\beta$ -NiOOH(s) via the oxidation process with the addition of Cu<sub>2</sub>O. At anodic peaks around 0.95 V, the electrodes demonstrated varying peak current densities, highlighting their catalytic activity. Flower Cu<sub>2</sub>O/NF had the highest peak current density at 4.6 mA cm<sup>-2</sup>, followed by particle Cu<sub>2</sub>O/NF at 3.1 mA cm<sup>-2</sup>, sheet Cu<sub>2</sub>O/NF at 2.2 mA cm<sup>-2</sup>, and NF at 1.2 mA cm<sup>-2</sup>. This order reveals that the presence of Cu<sub>2</sub>O in combination with NF significantly enhances catalytic activity. In terms of onset potential, it decreased from 0.75 V (for the NF electrode) to 0.55 V for all Cu<sub>2</sub>O/NF electrodes. This indicates an increase in the NF electrode's activity towards AOR with the introduction of Cu<sub>2</sub>O electrocatalysts.

Co and its composites, which are equally as extensively utilized as Ni, were also the subject of research due to their exceptional  $H_2$  production activity, high electrical conductivity, and durability. After that, the introduction of Co into Ni-C resulted in an improvement in AOR through the reduction of oxidation peaks within the potential range of 0.23–0.56 V, the augmentation of reversible metal-hydroxide production, and the generation of power ( $P_{\text{gen}}$ ) to maintain the reaction.<sup>48</sup> Greeley *et al.* concluded that, in addition to noble metals such as Pt and Ir, transition metals Ni and Co demonstrated high activities for HER.<sup>77</sup>

Metal oxides often suffer from insufficient activity and poor electrical conductivity. However, adding electronegative non-metals like phosphorus (P) and sulfur (S) can modify the electronic structure of transition metals and accelerate the surface reconstruction of the catalyst. The high electronegativity of S

attracts electrons from the outer layer of the transition metal. This attraction lowers the energy barrier for reaction intermediates, thereby enhancing the catalytic properties. This approach also significantly enhances the electrical conductivity of the catalysts. For example, a heterostructured electrocatalyst,  $\text{Ni}_3\text{S}_4@\text{NiCo}_2\text{O}_4/\text{NF}$ , was synthesized using the hydrothermal method for the AOR reaction.<sup>54</sup> Electrochemical tests indicated that the heterostructure of  $\text{Ni}_3\text{S}_4$  and  $\text{NiCo}_2\text{O}_4$  enhanced both the electrocatalytic activity and electrical conductivity compared to single-component catalysts, which demonstrated the highest current response and the lowest onset potential of 0.63 V vs. Hg/HgO at the current density of  $50 \text{ mA cm}^{-2}$ . *In situ* Raman spectroscopy revealed that during the AOR process, the surface of the heterostructured catalyst underwent significant reconstruction, forming  $\gamma\text{-NiOOH}$  with a more loose and disordered structure. Additionally, the  $\text{NiCo}_2\text{O}_4$  phase facilitated reconstruction at lower potentials. DFT calculations demonstrated that electron transfer within the heterostructured catalysts accelerated the reconstruction process and reduced the energy barriers for  $\text{Ni}_3\text{S}_4$  and  $\text{NiCo}_2\text{O}_4$  in the  $^*\text{NHNH}_2$  generation step. This promoted  $\text{NH}_3$  adsorption and  $\text{N}_2$  desorption, resulting in excellent AOR performance and following the G–M mechanism. The production of  $\text{N}_2$  in the AOR process represents a rapid energy release mechanism that effectively mitigates critical catalyst poisoning issues.

Recently, engineering confined transition metal nitride nanostructures offers an effective approach to directly control the  $\text{NH}_3$  adsorption/desorption process. This is facilitated by their tunable metal composition, excellent conductivity, high corrosion resistance, and large surface area. For example, after conducting electrochemical measurements, it was determined that the 1D nanoneedle Ni– $\text{Co}_2\text{N}$  electrode exhibited favourable surface area and active sites. This was demonstrated by its near-zero  $\text{H}_2$  evolution onset potential, 74 mV overpotential at  $10 \text{ mA cm}^{-2}$ , 138 mV at  $100 \text{ mA cm}^{-2}$ , and  $67 \text{ mV dec}^{-1}$  Tafel slope.<sup>21</sup> Furthermore, it exhibited exceptional long-term stability, as evidenced by a marginal decrease in the rate of  $\text{H}_2$  production following a decade of chronoamperometry measurements. In addition, at  $100 \text{ mA cm}^{-2}$ , the potential of  $\text{NH}_3$  electrolysis in a two-electrode system was 0.71 V, which was lower than that of water splitting. This indicates that the  $\text{H}_2$  produced from  $\text{NH}_3$  electrolysis may represent a viable alternative to water splitting. Interestingly, the incorporation of transition metal nitrides results in a downshift of the metal d-band center.<sup>78</sup> This effectively increases the antibonding electron density in the metal-adsorbate bond, potentially enabling electrocatalysts to achieve targeted moderate metal-adsorbate interactions through d-band contraction. Theoretical simulations indicate that the downshift of the metal d-band on nickel-cobalt nitride ( $\text{NiCo}_2\text{N}$ ) nanosheets helps maintain long-lasting AOR activity.<sup>15</sup> This is due to the moderate metal– $\text{NH}_3$  bond strength resulting from the d-band center downshift, optimizing key steps in AOR such as  $\text{NH}_3$  adsorption and  $^*\text{N}_2$  species desorption. Nitriding metals downshift metal d-bands and create empty  $e_g$  and  $t_{2g}$  states near the Fermi level. These empty states increase the oxidation states of the metal center and act as electron acceptors, reducing the barrier to generate  $\text{NH}_x^+$  cation radicals by facilitating fast electron transfer from the adsorbed  $\text{NH}_x$  to the high oxidation

state metal site.  $\text{NiCo}_2\text{N}$  nanosheets demonstrate lower charge transfer resistance ( $4.5 \Omega$ ) during AOR and a lower onset overpotential of 0.55 V.

Aside from that, the dendrite-like  $\text{NiCuBO}/\text{NF}$  demonstrates exceptional stability and electrocatalytic activity for AOR. Attainment of  $25 \text{ mA cm}^{-2}$  current density and a Tafel slope of  $63 \text{ mV dec}^{-1}$  for AOR requires a mere 1.301 V.<sup>49</sup> In a similar vein, boron nanoclusters deposited onto NiFe layered double hydroxide nanosheets ( $\text{B-NiFe-LDH}/\text{NF}$ ) demonstrated notable efficacy, as evidenced by a current density of  $100 \text{ mA cm}^{-2}$  and a voltage of 1.781 V, which is 202 mV lower than the voltage necessary for complete water splitting. Furthermore, after 24 hours of electrolysis, 78.6% of the  $\text{NH}_3$  was removed<sup>50</sup> (Fig. 12A and B). Furthermore, the utilization of density functional theory (DFT) simulation revealed that the formation of boron nanoclusters resulted in a reduction of the energy barrier, thereby promoting the  $\text{NH}_3$  adsorption–desorption process and the Volmer phase.

Fig. 13A illustrates that the effective AOR activity of TiO/Ti foil is demonstrated in an alkaline  $\text{NH}_3$  solution at a current density of  $0.06 \text{ mA cm}^{-2}$  and a voltage greater than 0.4 V.<sup>32</sup> The surface Vo in TiO is shown to significantly facilitate AOR activity through the reduction of the energy barrier in the rate-determining  $-\text{HNNH}_2$  formation phase and the promotion of  $\text{N}_2$  desorption, as demonstrated by density functional theory (DFT) calculations<sup>32</sup> (Fig. 13B). Defective  $\text{TiO}_2$  is a stable and cost-effective catalyst for

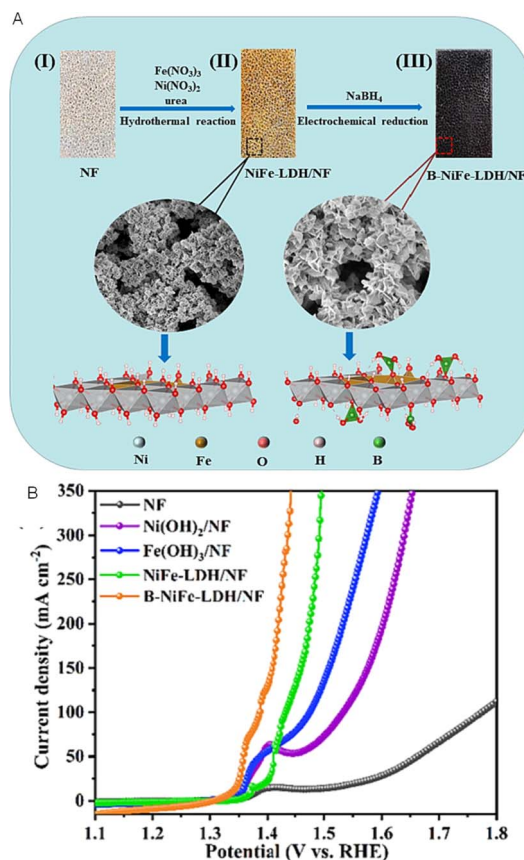


Fig. 12 (A) Schematic diagram and (B) LSV curve of B-NiFe-LDH/NF electrode. Reproduced from ref. 50 with permission from Elsevier, copyright 2023.

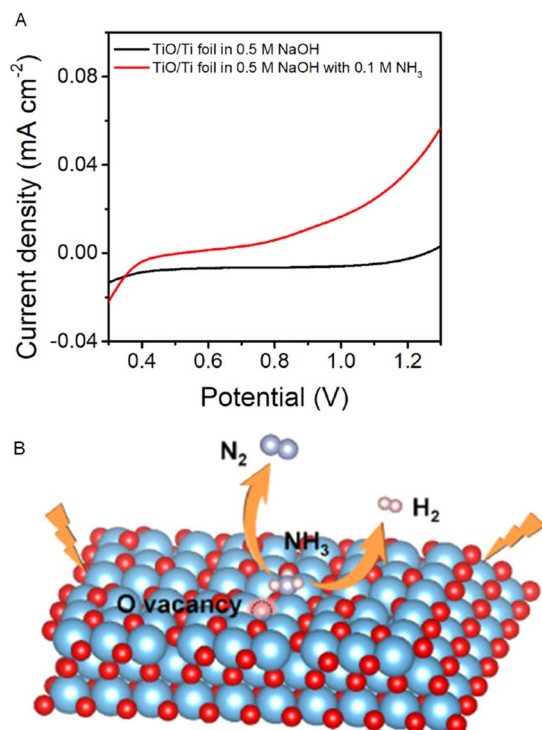


Fig. 13 (A) LSV curves of TiO/Ti foil in 0.5 M NaOH and 0.5 M NaOH with 0.1 M  $\text{NH}_3$  solution at a scan rate of  $10 \text{ mV s}^{-1}$  and (B) schematic diagram of AOR reaction in the presence of an oxygen vacancy on TiO surface. Reproduced from ref. 32 with permission from Elsevier, copyright 2021.

AOR, which is a potential electrode for efficient  $\text{H}_2$  production *via*  $\text{NH}_3$  electrolysis and direct  $\text{NH}_3$  fuel cells, as demonstrated by these results. Similarly, the  $\text{V}_\text{o}$  interfacial site is the main adsorption site for  $\text{NH}_3$ .<sup>79</sup> Aside from that, Khan *et al.* reported that the half-filled d-orbitals of Pd and Ru promoted  $\text{ZnO}/\text{Al}_2\text{O}_3$  ternary materials as effective and robust electrocatalysts towards AOR.<sup>47</sup> The current density was  $0.307 \text{ mA cm}^{-2}$  for  $\text{PdO}/\text{ZnO}/\text{Al}_2\text{O}_3$ , which was less than that of  $\text{MnO}_2/\text{ZnO}/\text{Al}_2\text{O}_3$ .

Perovskite oxides, represented by the formula  $\text{ABO}_3$ , are intriguing electrocatalysts due to their significant chemical and structural flexibility. In an ideal cubic system, the larger A-site is typically occupied by an alkaline-earth metal with 12-fold oxygen coordination, while the smaller B-site is occupied by a transition metal with 6-fold  $\text{BO}_6$  oxygen coordination. Zhang *et al.* investigated the use of Ni/Cu in the B-site of a stoichiometric  $\text{LaNi}_{0.5}\text{Cu}_{0.5}\text{O}_{3-\delta}$  perovskite as an AOR catalyst.<sup>55</sup> Their findings revealed that annealing the material in an argon atmosphere introduced  $\text{V}_\text{o}$ , which significantly enhanced its catalytic activity (onset potential of  $0.55 \text{ V vs. Ag/AgCl}$  at  $10 \text{ mA cm}^{-2}$ ). Similarly, Jeerh *et al.* investigated the optimal amount of Fe doping in  $\text{La}_{1-y}\text{Ni}_{0.6}\text{Cu}_{0.4-x}\text{Fe}_x\text{O}_{3-\delta}$  and discovered that  $\text{La}_{0.9}\text{Ni}_{0.6}\text{Cu}_{0.35}\text{Fe}_{0.05}\text{O}_{3-\delta}$  exhibited superior activity for the AOR.<sup>56</sup> This was evidenced by a lower onset potential of  $0.55 \text{ V vs. Ag/AgCl}$  at  $50 \text{ mA cm}^{-2}$ , attributed to the presence of  $\text{V}_\text{o}$  introduced by an A-site deficiency, which led to greater exposure of active  $\text{Ni}^{2+}$  on the surface. However, compared to the Zhang and co-workers' study,  $\text{La}_{0.5}\text{Sr}_{1.5}\text{Ni}_{0.9}\text{Cu}_{0.1}\text{O}_{4-\delta}$  can act as a robust AOR anode and achieve  $13.4 \text{ mA cm}^{-2}$  at a lower onset

potential of  $0.53 \text{ V vs. Ag/AgCl}$ .<sup>57</sup> The selective substitution of La with Sr enhances electronic conductivity and increases  $\text{V}_\text{o}$  concentration. Additionally, doping Cu into the B-site of the perovskite fosters a synergistic interaction between nickel and copper, leading to excellent AOR activity.

Fig. 14 shows the comparison of onset potential for various transition metal electrocatalysts for AOR. Among all catalysts,  $\text{RuO}_2\text{-ZnO}/\text{Al}_2\text{O}_3$  showed the lowest onset potential, followed by the  $\text{Ni}_{1-x}\text{Cu}_x\text{OOH}$ . The half-filled d-orbitals of Ru promoted  $\text{ZnO}/\text{Al}_2\text{O}_3$  ternary materials as effective and robust electrocatalysts towards AOR, meanwhile the abundant active sites and the synergistic effect between Ni and Cu, likely due to the formation of  $\text{Ni}_{1-x}\text{Cu}_x\text{OOH}$  on the surface of the catalysts through the electrochemical activation of the mixture of  $\text{Cu}(\text{OH})_2$  and  $\text{Ni}(\text{OH})_2$ . The perovskite oxide also shows a lower onset potential, which is likely due to the presence of  $\text{V}_\text{o}$ , which led to greater exposure of active  $\text{Ni}^{2+}$  on the surface. Most Ni-based Cu and Co show comparable onset potential for AOR reaction and the larger onset potential is B-NiFe-LDH/NF.

As a conclusion, both single-atom electrocatalysts and transition metal-based electrocatalysts have shown promising performance in  $\text{NH}_3$  electrooxidation. However, single-atom electrocatalysts offer several advantages over traditional transition metal-based catalysts, including higher catalytic activity, selectivity, and stability. The unique electronic and geometric structures of single-atom catalysts provide highly active and stable catalytic sites, leading to enhanced  $\text{NH}_3$  conversion efficiency and  $\text{H}_2$  production selectivity. Additionally, single-atom electrocatalysts can minimize the use of expensive transition metals, reducing production costs and improving the scalability of  $\text{NH}_3$  electrooxidation technology.

## Techno-economic analysis for $\text{NH}_3$ electrolysis

It is a promising alternative to use  $\text{NH}_3$  for the long-distance storage and transportation of  $\text{H}_2$  that is produced from renewable sources. An evaluation of the technological and economic

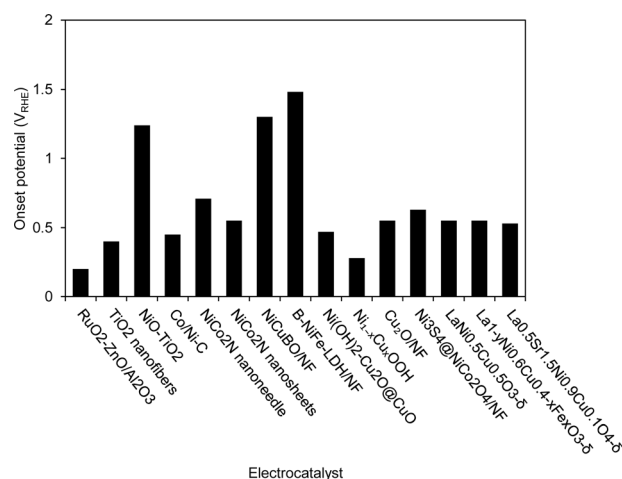


Fig. 14 Comparison of onset potential of various transition metal electrocatalysts under different current densities for AOR.

aspects was carried out to ascertain the levelized cost of H<sub>2</sub> (LCOH) that is produced from renewable NH<sub>3</sub> feedstocks as tabulated in Table 2. Lee *et al.* conducted a study in which they evaluated the costs that are connected with the thermal breakdown of NH<sub>3</sub> to produce H<sub>2</sub> at two distinct rates which are 0.9 m<sup>3</sup> h<sup>-1</sup> (0.08 kg h<sup>-1</sup>) for a laboratory scale and 30 m<sup>3</sup> h<sup>-1</sup> (2.67 kg h<sup>-1</sup>) for a small-scale H<sub>2</sub> refueling station.<sup>80</sup> They established a model of the process in their paper and verified its accuracy by comparing it to experimental findings reported by Chung *et al.*<sup>86</sup> The cost of H<sub>2</sub> production was assessed by the authors through the utilization of various economic methodologies, including sensitivity analysis, profitability analysis, and itemized cost estimation. By utilising itemised cost estimating and beginning with a green NH<sub>3</sub> pricing of 548 USD per tNH<sub>3</sub>, they were able to calculate that the LCOH on the laboratory scale was 9.97 USD per kgH<sub>2</sub>, while the LCOH on the refuelling station scale was 6.27 USD per kgH<sub>2</sub>.<sup>80</sup> These figures correspond to reconversion costs of 6.75 USD per kgH<sub>2</sub> and 3.14 USD per kgH<sub>2</sub>, respectively, when the cost of NH<sub>3</sub> feedstock is excluded from the LCOH calculation.

Nasharuddin *et al.* conducted a separate study in which they evaluated the technological and economic feasibility of NH<sub>3</sub> dissociation into H<sub>2</sub> for centralised installations (1000 kgH<sub>2</sub> d<sup>-1</sup>) and replenishment stations (500 kgH<sub>2</sub> d<sup>-1</sup>).<sup>81</sup> Due to differences in CAPEX and OPEX for both scales, the authors concluded that breaking NH<sub>3</sub> is economically viable for centralised H<sub>2</sub> production for 5.5 USD per kgH<sub>2</sub>.<sup>81</sup> On the other hand, the refuelling station is economically viable for 101 USD per kgH<sub>2</sub>. The price of NH<sub>3</sub> was 520 USD per tNH<sub>3</sub>, which the authors used as the basis for their study. Furthermore, Lin *et al.* devised a purification system to generate H<sub>2</sub> through thermal decomposition at an on-site H<sub>2</sub> refueling station supplied with NH<sub>3</sub> is 26.7 kg h<sup>-1</sup>.<sup>82</sup> Numerous purification configurations, including PSA, membrane, PSA-membrane, and others, were contrasted in terms of H<sub>2</sub> production costs by the authors. Beginning with an NH<sub>3</sub> cost of 540 USD per tNH<sub>3</sub>, the authors came to the conclusion that the PSA followed by the membrane purification system produces the most cost-effective H<sub>2</sub> production cost of 5.98 USD per kgH<sub>2</sub>.<sup>82</sup> This is equivalent to a reconversion cost of 0.91 USD per kgH<sub>2</sub>, which is the most affordable method of producing methane.

Furthermore, for large-scale H<sub>2</sub> production, comprehensive modeling was carried out by Makhoulfi and colleagues, who determined that the LCOH was 5.2 USD per kg.<sup>83</sup> This was

determined by assuming that the H<sub>2</sub> output rate was 7560 kg h<sup>-1</sup> and that the price of NH<sub>3</sub> was 488 USD per tNH<sub>3</sub>.<sup>83</sup> A techno-economic modeling study was undertaken by Lullo *et al.* to examine 32 H<sub>2</sub> transport systems, which comprised five fluids (hythane, gaseous H<sub>2</sub>, NH<sub>3</sub>, liquid H<sub>2</sub> and LOHC) and three modes of transportation (vehicle pipeline, and rail).<sup>84</sup> Following the simulation of the process, they concluded that the amount of thermal energy consumed was 4.38 GJ NG per tH<sub>2</sub>, while the amount of electrical energy consumed was 81 kW h per tH<sub>2</sub>. In their research, the cost of converting H<sub>2</sub> into H<sub>2</sub> (reconversion) was calculated to be 2.61 USD per kgH<sub>2</sub>.<sup>84</sup> Cesaro *et al.* assessed the expenses associated with generating electricity from NH<sub>3</sub> via various methods, including the conversion of NH<sub>3</sub> to H<sub>2</sub> for fuel cell applications.<sup>87</sup> To determine the energy efficiency and costs associated with the various routes of NH<sub>3</sub> thermal breakdown using a large-scale NH<sub>3</sub> refinery, a techno-economic assessment was carried out. After everything was said and done, they concluded that the levelized cost of energy would be anywhere between 167 and 197 USD per MW h at a plant capacity factor of 25%, presuming that NH<sub>3</sub> would cost 380 USD per tNH<sub>3</sub>.

Papadias *et al.* conducted an assessment of the expenses associated with utilizing various liquid H<sub>2</sub> carriers, such as toluene, methanol, and NH<sub>3</sub>, to transport H<sub>2</sub>.<sup>85</sup> At a rate of 50 tpd, the authors found that NH<sub>3</sub> had the highest production cost (2.2 USD per kgH<sub>2</sub>) and the lowest breakdown cost to H<sub>2</sub> (0.61 USD per kgH<sub>2</sub>).<sup>85</sup> According to the IEA's "The Future of H<sub>2</sub>" report, the anticipated cost of converting NH<sub>3</sub> to H<sub>2</sub> in a centralised facility (15 000 tNH<sub>3</sub> per year) would be 1 USD per kgH<sub>2</sub>. However, the report does not provide any specific assumptions regarding the reconversion process.<sup>88</sup>

In a recent study conducted by Kanaan *et al.*, the most economical ways to produce H<sub>2</sub> gas from NH<sub>3</sub> were found to be electrolysis while in transit, thermal decomposition using membrane technology at the import terminal, and a fixed bed at the H<sub>2</sub> refuelling station.<sup>89</sup> Given the significance of the capital cost in conducting the techno-economic assessment, it is imperative to determine the appropriate dimensions for each piece of equipment. They discovered that membrane reactor technology is currently the most cost-effective method for converting NH<sub>3</sub> to H<sub>2</sub> (7.72 USD per kgH<sub>2</sub>). The technology exhibits benefit in comparison to traditional fixed bed technologies by its reduced operational expenses. Electrolysis of NH<sub>3</sub> on a truck resulted in the lowest LCOH, at 9.59 USD per kgH<sub>2</sub>. Membrane technology has a somewhat higher LCOH (9.14 USD per kgH<sub>2</sub>) than fixed bed technology (8.69 USD per kgH<sub>2</sub>).<sup>19</sup> The variations in the process configurations for the various scales account for this. The cost of H<sub>2</sub> gas produced at the import terminal using fixed bed and membrane technology is competitive in terms of LCOH, especially when compared to the current green H<sub>2</sub> pricing in Europe, which are 4–8 USD per kgH<sub>2</sub>, according to the IEA.

Table 2 Techno-economic for H<sub>2</sub> production via AOR

| Method                        | Cost of H <sub>2</sub> production (USD per kgH <sub>2</sub> ) | Ref. |
|-------------------------------|---|------|
| Thermal decomposition         | 9.97  | 80   |
| Thermal decomposition         | 5.5   | 81   |
| Membrane purification         | 5.98  | 82   |
| Fired NH <sub>3</sub> cracker | 5.2   | 83   |
| Thermal decomposition         | 2.61  | 84   |
| Thermal decomposition         | 2.2   | 85   |
| Membrane technology           | 7.72  | 19   |
| Electrolysis                  | 9.59  |      |
| Fixed bed technology          | 8.69  |      |

## Summary, future perspectives, and recommendations

Electrocatalysts play a crucial role in the electrooxidation of NH<sub>3</sub> for clean H<sub>2</sub> production. With the increasing demand for

renewable energy sources, electrocatalysis has emerged as a promising method for efficient and sustainable H<sub>2</sub> production. NH<sub>3</sub>, with its high H<sub>2</sub> content, has gained attention as a potential carrier for H<sub>2</sub>. However, the electrooxidation of NH<sub>3</sub> faces challenges such as low conversion efficiency, poor selectivity, and catalyst degradation. The commercialization of AOR relies on the development of robust and efficient electrocatalysts. Because of their high NH<sub>3</sub> affinity and fast AOR kinetics, Pt electrocatalysts have been investigated in depth using a variety of techniques, including alloying, surface morphology modification, and electrocatalytic reaction optimization. In particular, by successfully lowering the energy barrier, a Pt–Ir greatly enhanced the reaction kinetics of AOR.

There has been a lot of talk about using cheaper, non-noble metal catalysts, especially catalysts based on nickel, as a substitute for Pt. When the affinity of NH<sub>3</sub> and intermediates on Ni and Cu was changed, the Ni–Cu bimetal catalysts showed the most promising activity in terms of reaction rate and stability. Nevertheless, the development of potent new catalysts and their continued search for are essential for the practical implementation of AOR. Particularly to develop non-noble metal electrocatalysts for AOR that are economical, several obstacles must be surmounted. Initially, selective AOR in regions with minimal overpotential is critical. Alternatively, AOR competes with competing reactions such as water oxidation, NH<sub>3</sub> oxidation to NO<sub>3</sub><sup>−</sup> or NO<sub>2</sub>, and so on, while traditional electrocatalysts based on non-noble metals showed AOR performance at high overpotentials. Conversely, it was discovered that the introduction of heteroatoms into alloys can modify the electronic configuration of catalysts, leading to a decrease in the energy barrier for NH<sub>3</sub> adsorption and eventually a reduction in the overpotential.

Improving AOR requires not just creating catalysts, but also a basic understanding of the reaction mechanism. At present, the AOR mechanism is primarily being studied in relation to its applicability to Pt catalysts. Nevertheless, the specific rate-determining steps or reaction mechanisms may vary among distinct electrocatalyst types. The DFT calculations have been extensively utilized in order to delineate the fundamental effect of the catalytic modification and to propose reaction mechanisms. In light of developments in theoretical inquiry, experimental observation of reaction mechanisms through the monitoring of adsorbed intermediates has become crucial. Recent studies have documented endeavors to examine the true mechanisms of action on electrocatalysts through the utilization of *in situ* or *operando* characterizations. In light of the advancements made thus far, the AOR possesses considerable practical development potential through the integration of device engineering, catalytic modification, and fundamental research.

The replacement of water with liquid NH<sub>3</sub> is another feature that could revolutionize AOR technology for fuel cells. NH<sub>3</sub> only becomes corrosive when reacting with water to generate the caustic OH<sup>−</sup>, however, this gas has a far larger energy density and is resistant to pipeline corrosion. The challenges associated with water oxidation are eliminated when a nonaqueous electrolyte is combined with liquid NH<sub>3</sub>. Furthermore, it is critical

to conduct further mechanistic investigations on nonaqueous liquid NH<sub>3</sub>, given its considerable potential provided that the challenges impeding its application in AOR can be resolved. Aside from this, the efficient energy generation *via* direct NH<sub>3</sub> fuel cells and the electrochemical synthesis of “green NH<sub>3</sub>” presents a highly promising pathway towards carbon neutrality by 2050.

## Data availability

The data that support the findings of this study are available from the corresponding author upon reasonable request. Please note that due to confidentiality agreements, certain restrictions apply to the availability of the data.

## Conflicts of interest

The authors stated that there are no known conflicts of interest in this article.

## Acknowledgements

The authors are gratefully acknowledging to the Universiti Teknologi Malaysia for the Fundamental Research Grant (No. 22H51) and Professional Development Research University Grant (No. 06E92 and PY/2024/00993).

## References

- 1 J. A. Okolie, B. R. Patra, A. Mukherjee, S. Nanda, A. K. Dalai and J. A. Kozinski, *Int. J. Hydrogen Energy*, 2021, **46**, 8885–8905.
- 2 A. Kovač, M. Paranos and D. Marciuš, *Int. J. Hydrogen Energy*, 2021, **46**, 10016–10035.
- 3 S. Anwar, F. Khan, Y. Zhang and A. Djire, *Int. J. Hydrogen Energy*, 2021, **46**, 32284–32317.
- 4 L. Cao, I. K. M. Yu, X. Xiong, D. C. W. Tsang, S. Zhang, J. H. Clark, C. Hu, Y. H. Ng, J. Shang and Y. S. Ok, *Environ. Res.*, 2020, **186**, 109547.
- 5 G. Franchi, M. Capocelli, M. De Falco, V. Piemonte and D. Barba, *Membranes*, 2020, **10**, 10.
- 6 S. A. Lee, M. G. Lee and H. W. Jang, *Sci. China Mater.*, 2022, **65**, 3334–3352.
- 7 J. Łuczak and M. Lieder, *Adv. Colloid Interface Sci.*, 2023, **319**, 102963.
- 8 Y. Tian, Z. Mao, L. Wang and J. Liang, *Small Struct.*, 2023, **4**, 2200266.
- 9 K. Siddharth, Y. Hong, X. Qin, H. J. Lee, Y. T. Chan, S. Zhu, G. Chen, S.-I. Choi and M. Shao, *Appl. Catal., B*, 2020, **269**, 118821.
- 10 F. Almomani, R. Bhosale, M. Khraisheh, A. Kumar and M. Tawalbeh, *Int. J. Hydrogen Energy*, 2020, **45**, 10398–10408.
- 11 R. Wang, H. Liu, K. Zhang, G. Zhang, H. Lan and J. Qu, *Chem. Eng. J.*, 2021, **404**, 126795.
- 12 M.-H. Tsai, T.-C. Chen, Y. Juang, L.-C. Hua and C. Huang, *Electrochem. Commun.*, 2020, **121**, 106875.

- 13 F. Quan, G. Zhan, B. Zhou, C. Ling, X. Wang, W. Shen, J. Li, F. Jia and L. Zhang, *J. Environ. Sci.*, 2023, **125**, 544–552.
- 14 J. R. Barbosa, M. N. Leon, C. M. Fernandes, R. M. Antoniassi, O. C. Alves, E. A. Ponzio and J. C. M. Silva, *Appl. Catal., B*, 2020, **264**, 118458.
- 15 S. He, Y. Chen, M. Wang, H. Nuomin, P. Novello, X. Li, S. Zhu and J. Liu, *Nano Energy*, 2021, **80**, 105528.
- 16 Z.-H. Lyu, J. Fu, T. Tang, J. Zhang and J.-S. Hu, *EnergyChem*, 2023, **5**, 100093.
- 17 J. H. Jang, S. Y. Park, D. H. Youn and Y. J. Jang, *Catalysts*, 2023, **13**, 803.
- 18 P. Peng, J. Su and H. Breunig, *Energy Convers. Manage.*, 2023, **288**, 117166.
- 19 R. Kanaan, P. H. Affonso Nóbrega, P. Achard and C. Beauger, *Renewable Sustainable Energy Rev.*, 2023, **188**, 113784.
- 20 H. Mashhadimoslem, M. Safarzadeh Khosrowshahi, M. Delpisheh, C. Convery, M. Rezakazemi, T. M. Aminabhavi, M. Kamkar and A. Elkamel, *Chem. Eng. J.*, 2023, **474**, 145661.
- 21 K. Jiang, K. Li, Y.-Q. Liu, S. Lin, Z. Wang, D. Wang and Y. Ye, *Electrochim. Acta*, 2022, **403**, 139700.
- 22 N. Hassan, A. Jalil, N. Khusnun, A. Ahmad, T. Abdullah, R. Kasmani, N. Norazahar, M. Kamaroddin and D. Vo, *Environ. Chem. Lett.*, 2022, 1–23.
- 23 M. Sawal, A. Jalil, T. Abdullah, N. Khusnun, N. Hassan, F. Aziz, A. Fauzi, M. Kamaroddin, M. Omar and S. Haron, *Energy Convers. Manage.*, 2022, **274**, 116456.
- 24 X. Yang, H. Sun, C. Liu, L. Yu and H. Chen, *Chem. Eng. J.*, 2022, **442**, 136167.
- 25 N. M. Adli, H. Zhang, S. Mukherjee and G. Wu, *J. Electrochem. Soc.*, 2018, **165**, J3130–J3147.
- 26 Y. Tian, H. Tan, X. Li, J. Jia, Z. Mao, J. Liu and J. Liang, *Chin. J. Catal.*, 2024, **56**, 25–50.
- 27 H. Kim, S. Hong, H. Kim, Y. Jun, S. Y. Kim and S. H. Ahn, *Appl. Mater. Today*, 2022, **29**, 101640.
- 28 K. Siddharth, Y. Chan, L. Wang and M. Shao, *Curr. Opin. Electrochem.*, 2018, **9**, 151–157.
- 29 X. Jiang, D. Ying, X. Liu, M. Liu, S. Zhou, C. Guo, G. Zhao, Y. Wang and J. Jia, *Electrochim. Acta*, 2020, **345**, 136157.
- 30 J. Huang, Z. Chen, J. Cai, Y. Jin, T. Wang and J. Wang, *Nano Res.*, 2022, **15**, 5987–5994.
- 31 X. Yang, L. Sun, X. Liu, Z. Yang, H. Sun, W. Liu and H. Chen, *ACS Catal.*, 2024, **14**, 6236–6246.
- 32 S. Zhang, Y. Zhao, L. Yan, H. Jiang, X. Yang, Y. Wang, H. Song and X. Zhao, *Int. J. Hydrogen Energy*, 2021, **46**, 39208–39215.
- 33 N. Akagi, K. Hori, H. Sugime, S. Noda and N. Hanada, *J. Catal.*, 2022, **406**, 222–230.
- 34 D. T. Tran, T. H. Nguyen, H. Jeong, P. K. L. Tran, D. Malhotra, K. U. Jeong, N. H. Kim and J. H. Lee, *Nano Energy*, 2022, **94**, 106929.
- 35 C. Jo, S. Surendran, M.-C. Kim, T.-Y. An, Y. Lim, H. Choi, G. Janani, S. Cyril Jesudass, D. Jun Moon, J. Kim, J. Young Kim, C. Hyuck Choi, M. Kim, J. Kyu Kim and U. Sim, *Chem. Eng. J.*, 2023, **463**, 142314.
- 36 J. H. Jang, S. Y. Park, D. H. Youn and Y. J. Jang, *Catalysts*, 2023, **13**, 803.
- 37 J. Liu, W. Hu, C. Zhong and Y. F. Cheng, *J. Power Sources*, 2013, **223**, 165–174.
- 38 N. N. Fomena, S. Garbarino, E. Bertin, A. Korinek, G. Botton, L. Roué and D. Guay, *J. Catal.*, 2017, **354**, 270–277.
- 39 V. A. Ribeiro, I. C. de Freitas, A. O. Neto, E. V. Spinacé and J. C. M. Silva, *Mater. Chem. Phys.*, 2017, **200**, 354–360.
- 40 X. Lin, X. Zhang, Z. Wang, X. Zhu, J. Zhu, P. Chen, T. Lyu, C. Li, Z. Q. Tian and P. K. Shen, *J. Colloid Interface Sci.*, 2021, **601**, 1–11.
- 41 H. Yang, X. Huang, Z. Liu, X. Lin, Q. Chen, J. Li, C. Zhang, Z. P. Kan, Z. Q. Tian and P. K. Shen, *J. Colloid Interface Sci.*, 2023, **652**, 1764–1774.
- 42 J. C. M. Silva, S. Ntais, É. Teixeira-Neto, E. V. Spinacé, X. Cui, A. O. Neto and E. A. Baranova, *Int. J. Hydrogen Energy*, 2017, **42**, 193–201.
- 43 J. Jiang, *Electrochem. Commun.*, 2017, **75**, 52–55.
- 44 S. Ntais, A. Serov, N. I. Andersen, A. J. Roy, E. Cossar, A. Allagui, Z. Lu, X. Cui, E. A. Baranova and P. Atanassov, *Electrochim. Acta*, 2016, **222**, 1455–1463.
- 45 L. L. Sikeyi, L. R. Bila, T. D. Ntuli, C. T. Selepe, N. W. Maxakato, N. J. Coville and M. S. Maubane-Nkadimeng, *Diamond Relat. Mater.*, 2023, **132**, 109612.
- 46 J.-J. Zhong, S.-P. Huang, J.-F. Gu, Y. Li, K.-N. Ding, Y.-F. Zhang, W. Lin and W.-K. Chen, *Appl. Surf. Sci.*, 2023, **609**, 155280.
- 47 S. Khan, S. S. Shah, A. B. Yurtcan, A. A. A. Bahajjaj, A. Zafar and N. K. Janjua, *Fuel*, 2023, **347**, 128446.
- 48 F. Almomani and M. A. H. S. Saad, *Int. J. Hydrogen Energy*, 2021, **46**, 4678–4690.
- 49 A. A. Kashale, C.-T. Wu, H.-F. Hsu and I.-W. P. Chen, *Chem. Eng. J.*, 2023, **474**, 145907.
- 50 J. Wang, S. Qing, X. Tong, K. Zhang, G. Luo, J. Ding and L. Xu, *Appl. Surf. Sci.*, 2023, **640**, 158330.
- 51 J. Huang, J. Cai and J. Wang, *ACS Appl. Energy Mater.*, 2020, **3**, 4108–4113.
- 52 W. Xu, R. Lan, D. Du, J. Humphreys, M. Walker, Z. Wu, H. Wang and S. Tao, *Appl. Catal., B*, 2017, **218**, 470–479.
- 53 M.-H. Tsai, Y. Juang, C.-C. Hu, L.-C. Hua and C. Huang, *J. Environ. Chem. Eng.*, 2024, **12**, 112339.
- 54 L. Wang, K. Jiang, Z. Wang, T. Li, D. Wang and Y.-Q. Liu, *Chem. Eng. J.*, 2024, **492**, 152268.
- 55 M. Zhang, H. Li, X. Duan, P. Zou, G. Jeerh, B. Sun, S. Chen, J. Humphreys, M. Walker and K. Xie, *Adv. Sci.*, 2021, **8**, 2101299.
- 56 G. Jeerh, P. Zou, M. Zhang, S. Chen, J. Humphreys and S. Tao, *Sep. Purif. Technol.*, 2022, **297**, 121451.
- 57 M. Zhang, P. Zou, G. Jeerh, B. Sun, M. Walker and S. Tao, *Adv. Funct. Mater.*, 2022, **32**, 2204881.
- 58 H. Li, W. Wang, S. Xue, J. He, C. Liu, G. Gao, S. Di, S. Wang, J. Wang and Z. Yu, *J. Am. Chem. Soc.*, 2024, **146**, 9124–9133.
- 59 H. Li, S. Di, P. Niu, S. Wang, J. Wang and L. Li, *Energy Environ. Sci.*, 2022, **15**, 1601–1610.
- 60 C. Liu, F. Yang, A. Schechter and L. Feng, *Adv. Sens. Energy Mater.*, 2023, 100055.
- 61 F. J. Vidal-Iglesias, J. Solla-Gullón, V. Montiel, J. Feliu and A. Aldaz, *J. Power Sources*, 2007, **171**, 448–456.

- 62 H. S. Pillai and H. Xin, *Ind. Eng. Chem. Res.*, 2019, **58**, 10819–10828.
- 63 C. Xiao, B.-A. Lu, P. Xue, N. Tian, Z.-Y. Zhou, X. Lin, W.-F. Lin and S.-G. Sun, *Joule*, 2020, **4**, 2562–2598.
- 64 F. J. Vidal-Iglesias, J. Solla-Gullón, P. Rodriguez, E. Herrero, V. Montiel, J. Feliu and A. Aldaz, *Electrochem. Commun.*, 2004, **6**, 1080–1084.
- 65 S. Johnston, B. H. Suryanto and D. R. MacFarlane, *Electrochim. Acta*, 2019, **297**, 778–783.
- 66 J. Zhou, J. S. Chung and S. G. Kang, *Int. J. Hydrogen Energy*, 2024, **58**, 745–752.
- 67 M. H. Assumpção, S. G. da Silva, R. F. de Souza, G. S. Buzzo, E. V. Spinacé, A. O. Neto and J. C. M. Silva, *Int. J. Hydrogen Energy*, 2014, **39**, 5148–5152.
- 68 M. H. Assumpção, R. M. Piasentin, P. Hammer, R. F. De Souza, G. S. Buzzo, M. C. Santos, E. V. Spinacé, A. O. Neto and J. C. M. Silva, *Appl. Catal., B*, 2015, **174**, 136–144.
- 69 T. L. Lomocoso and E. A. Baranova, *Electrochim. Acta*, 2011, **56**, 8551–8558.
- 70 Q. Xue, Y. Zhao, J. Zhu, Y. Ding, T. Wang, H. Sun, F. Li, P. Chen, P. Jin and S. Yin, *J. Mater. Chem. A*, 2021, **9**, 8444–8451.
- 71 A. Estejab and G. G. Botte, *Mol. Catal.*, 2018, **445**, 279–292.
- 72 Y. Li, X. Li, H. S. Pillai, J. Lattimer, N. Mohd Adli, S. Karakalos, M. Chen, L. Guo, H. Xu and J. Yang, *ACS Catal.*, 2020, **10**, 3945–3957.
- 73 A. Allagui, S. Sarfraz and E. A. Baranova, *Electrochim. Acta*, 2013, **110**, 253–259.
- 74 K. Yao and Y. Cheng, *Mater. Chem. Phys.*, 2008, **108**, 247–250.
- 75 J. Łuczak and M. Lieder, *Adv. Colloid Interface Sci.*, 2023, 102963.
- 76 W. Xu, D. Du, R. Lan, J. Humphreys, D. N. Miller, M. Walker, Z. Wu, J. T. Irvine and S. Tao, *Appl. Catal., B*, 2018, **237**, 1101–1109.
- 77 J. Greeley, T. F. Jaramillo, J. Bonde, I. Chorkendorff and J. K. Nørskov, *Nat. Mater.*, 2006, **5**, 909–913.
- 78 D. J. Little, D. O. Edwards, M. R. Smith III and T. W. Hamann, *ACS Appl. Mater. Interfaces*, 2017, **9**, 16228–16235.
- 79 H. Sun, H. Wang and Z. Qu, *ACS Catal.*, 2023, **13**, 1077–1088.
- 80 B. Lee, J. Park, H. Lee, M. Byun, C. W. Yoon and H. Lim, *Renewable Sustainable Energy Rev.*, 2019, **113**, 109262.
- 81 R. Nasharuddin, M. Zhu, Z. Zhang and D. Zhang, *Int. J. Hydrogen Energy*, 2019, **44**, 14445–14455.
- 82 L. Lin, Y. Tian, W. Su, Y. Luo, C. Chen and L. Jiang, *Sustainable Energy Fuels*, 2020, **4**, 3006–3017.
- 83 C. Makhouloufi and N. Kezibri, *Int. J. Hydrogen Energy*, 2021, **46**, 34777–34787.
- 84 G. Di Lullo, T. Giwa, A. Okunlola, M. Davis, T. Mehedi, A. Oni and A. Kumar, *Int. J. Hydrogen Energy*, 2022, **47**, 35293–35319.
- 85 D. D. Papadias, J.-K. Peng and R. K. Ahluwalia, *Int. J. Hydrogen Energy*, 2021, **46**, 24169–24189.
- 86 D. B. Chung, H. Y. Kim, M. Jeon, D. H. Lee, H. S. Park, S. H. Choi, S. W. Nam, S. C. Jang, J.-H. Park and K.-Y. Lee, *Int. J. Hydrogen Energy*, 2017, **42**, 1639–1647.
- 87 Z. Cesaro, M. Ives, R. Nayak-Luke, M. Mason and R. Bañares-Alcántara, *Appl. Energy*, 2021, **282**, 116009.
- 88 IEA, *The Future Hydrogen*, 2019, DOI: [10.1787/1e0514c4-en](https://doi.org/10.1787/1e0514c4-en).
- 89 R. Kanaan, P. H. A. Nóbrega, P. Achard and C. Beauger, *Renewable Sustainable Energy Rev.*, 2023, **188**, 113784.